Monthly Notices
of the
ROYAL ASTRONOMICAL SOCIETY

Mon. Not. R. Astron. Soc. **402,** 191–206 (2010) doi:10.1111/j.1365-2966.2009.15914.x

Halo mass function and scale-dependent bias from *N*-body simulations with non-Gaussian initial conditions

Annalisa Pillepich,[1⋆] Cristiano Porciani[1,2] and Oliver Hahn[1]

[1]*Institute for Astronomy, ETH Zurich, 8093 Zurich, Switzerland*
[2]*Argelander Institut für Astronomie, Auf dem Hügel 71, D-53121, Germany*

Accepted 2009 October 22. Received 2009 July 17; in original form 2008 November 26

ABSTRACT

We perform a series of high-resolution *N*-body simulations of cosmological structure formation starting from Gaussian and non-Gaussian initial conditions. We adopt the best-fitting cosmological parameters from the third- and fifth-year data releases of the *Wilkinson Microwave Anisotropy Probe,* and we consider non-Gaussianity of the local type parametrized by eight different values of the non-linearity parameter $f_{\rm NL}$. Building upon previous work based on the Gaussian case, we show that, when expressed in terms of suitable variables, the mass function of friends-of-friends haloes is approximately universal (i.e. independent of redshift, cosmology and matter transfer function) to good precision (nearly 10 per cent) also in non-Gaussian scenarios. We provide fitting formulae for the high-mass end ($M > 10^{13}\,h^{-1}\,{\rm M}_\odot$) of the universal mass function in terms of $f_{\rm NL}$, and we also present a non-universal fit in terms of both $f_{\rm NL}$ and z to be used for applications requiring higher accuracy. For Gaussian initial conditions, we extend our fit to a wider range of halo masses ($M > 2.4 \times 10^{10}\,h^{-1}\,{\rm M}_\odot$) and we also provide a consistent fit of the linear halo bias. We show that, for realistic values of $f_{\rm NL}$, the matter power spectrum in non-Gaussian cosmologies departs from the Gaussian 1 by up to 2 per cent on the scales where the baryonic-oscillation features are imprinted on the two-point statistics. Finally, using both the halo power spectrum and the halo-matter cross spectrum, we confirm the strong k-dependence of the halo bias on large scales ($k < 0.05\,h\,{\rm Mpc}^{-1}$) which was already detected in previous studies. However, we find that commonly used parametrizations based on the peak-background split do not provide an accurate description of our simulations which present extra dependencies on the wavenumber, the non-linearity parameter and, possibly, the clustering strength. We provide an accurate fit of the simulation data that can be used as a benchmark for future determinations of $f_{\rm NL}$ with galaxy surveys.

Key words: methods: *N*-body simulations – galaxies: clusters: general – galaxies: haloes – cosmology: theory – dark matter – large-scale structure of Universe.

1 INTRODUCTION

The detection of temperature anisotropies in the cosmic microwave background (CMB) provided evidence that large-scale structure formation in the Universe was seeded by small density fluctuations generated at early times. The statistical properties of these seeds are usually modelled with a Gaussian random field. Historically, the Gaussian approximation was introduced for mathematical convenience. In the absence of a solid model for the generation of density fluctuations, the Gaussian hypothesis was accepted on the basis of the central limit theorem (e.g. Bardeen et al. 1986 and references therein). The advent of inflationary models provided further support for Gaussianity. Small-amplitude curvature perturbations generated during a standard inflationary phase (single field, slow roll) are very nearly Gaussian distributed (e.g. Bartolo et al. 2004 and references therein).

However, many variants of the inflationary scenario predict appreciable levels of primordial non-Gaussianity. In terms of Bardeen's gauge-invariant potential, Φ, most of these models (but not all, see e.g. Creminelli, Senatore & Zaldarriaga 2007) can be reduced to the form:

$$\Phi = \phi + f_{\rm NL}(\phi^2 - \langle\phi^2\rangle)\,, \qquad (1)$$

where ϕ is an auxiliary Gaussian random field and $f_{\rm NL}$ quantifies the amount of primordial non-Gaussianity. On subhorizon scales, $\Phi = -\Psi$, where Ψ denotes the usual peculiar gravitational potential related to density fluctuations via Poisson's equation. The

⋆E-mail: annalisa@phys.ethz.ch

parameter $f_{\rm NL}$ thus has the same sign as the skewness of the density probability distribution function. This local form of non-Gaussianity (note that equation 1 applies in configuration space) can be obtained from a truncated expansion of the effective inflaton potential (Salopek & Bond 1990; Falk, Rangarajan & Srednicki 1993; Gangui et al. 1994). The parameter $f_{\rm NL}$ thus encodes information about the inflaton physics. Standard inflation gives $|f_{\rm NL}| \ll 1$ (Salopek & Bond 1990; Maldacena 2003). However, even in this case, the non-linear evolution of perturbations on superhorizon scales yields an observable $f_{\rm NL}$ of order unity (which, in reality, should be scale and redshift dependent; Bartolo, Matarrese & Riotto 2005; see also Pyne & Carroll 1996). Large values of $|f_{\rm NL}|$ naturally arise in multifield inflation models (e.g. Linde & Mukhanov 1997; for an extensive review see Bartolo et al. 2004) and even in cyclic or ekpyrotic models of the universe with no inflation (Creminelli & Senatore 2007; Buchbinder, Khoury & Ovrut 2008; Lehners & Steinhardt 2008).

Observational constraints on $f_{\rm NL}$ have been derived studying three-point statistics of temperature fluctuations in the CMB (Komatsu & Spergel 2001). The recent 5-yr data from the *Wilkinson Microwave Anisotropy Probe* (*WMAP*) give $-9 < f_{\rm NL} < 111$ at the 95 per cent confidence level (Komatsu et al. 2008). Parallel studies on the same data set give $-178 < f_{\rm NL} < 64$ using Minkowski functionals (Komatsu et al. 2008) and $-8 < f_{\rm NL} < 111$ from wavelet decomposition (Curto et al. 2008). Some recent re-analyses of earlier 3-yr *WMAP* data claim substantial evidence for positive $f_{\rm NL}$: $27 < f_{\rm NL} < 147$ from the bispectrum of temperature fluctuations (Yadav & Wandelt 2008) and $23 < f_{\rm NL} < 75$ from their one-point distribution function (Jeong & Smoot 2007). On the other hand, a study of Minkowski functionals on the 3-yr data gives $-70 < f_{\rm NL} < 91$ (Hikage et al. 2008). Higher quality data are needed to improve these constraints. The upcoming Planck satellite should be able to reduce the uncertainty in $f_{\rm NL}$ to $\sim$5 (Komatsu & Spergel 2001).

Alternatively, one might use observational signatures of primordial non-Gaussianity imprinted in the large-scale structure (LSS) of the Universe (e.g. Moscardini et al. 1991). Ideally, one would like to use high-redshift probes as the non-linear growth of density fluctuations quickly superimposes a strong non-Gaussian signal on to the primordial one so that the latter might then be difficult to recover. For instance, the large-scale distribution of neutral hydrogen in the era between hydrogen recombination and reionization encodes information on $f_{\rm NL}$ (Pillepich, Porciani & Matarrese 2007). This could be probed by detecting the redshifted hyperfine 21-cm transition with very low-frequency radio arrays from space. In principle, an experiment of this kind can limit $f_{\rm NL}$ to $\Delta f_{\rm NL} < 1$ (Pillepich et al. 2007, see also Cooray 2006). However, it is not clear yet whether such an experiment will ever be possible due to technical complexity and problematic foreground subtraction. At lower redshifts, $f_{\rm NL}$ can be constrained probing the statistics of rare events, as like as the mass function of galaxy groups and clusters (Matarrese, Lucchin & Bonometto 1986; Matarrese, Verde & Jimenez 2000; Koyama, Soda & Taruya 1999; Robinson & Baker 2000; Robinson, Gawiser & Silk 2000; LoVerde et al 2008). Early attempts of using cluster counts to constrain $f_{\rm NL}$ have been rather inconclusive due to low-number statistics (see e.g. Willick 2000; Amara & Refregier 2004 and references therein). Even though cluster-mass estimates are still rather uncertain and massive objects are very rare, the observational perspectives look very promising. A number of galaxy surveys encompassing large fractions of the observable Universe are being planned [e.g. ground-based surveys as Dark Energy Survey (DES), Panoramic Survey Telescope & Rapid Response System (PanSTARRS) and Large Synoptic Survey Telescope (LSST), and the satellite missions EUCLID and Advanced Dark Energy Physics Telescope (ADEPT)] and could potentially lead to solid measurements of $f_{\rm NL}$ (e.g. Carbone, Verde & Matarrese 2008; Dalal et al. 2008).

Primordial non-Gaussianity is also expected to modify the clustering properties of massive cosmic structures forming out of rare density fluctuations (Grinstein & Wise 1986; Matarrese et al. 1986; Lucchin, Matarrese & Vittorio 1988; Koyama, Soda & Taruya 1999). Also in this case, however, the non-linear evolution of the mass density generally superimposes a stronger signal than that generated by primordial non-Gaussianity on to the galaxy three-point statistics. The galaxy bispectrum is thus sensitive to $f_{\rm NL}$ only at high redshift (Verde et al. 2000; Scoccimarro, Sefusatti & Zaldarriaga 2004; Sefusatti & Komatsu 2007).

Recently, Dalal et al. (2008) have shown analytically that primordial non-Gaussianity of the local type is expected to generate a scale-dependent large-scale bias in the clustering properties of massive dark-matter haloes. This is a consequence of the fact that large and small-scale density fluctuations are not independent when $f_{\rm NL} \neq 0$. Similar calculations have been presented by Matarrese & Verde (2008), Slosar et al. (2008), Afshordi & Tolley (2008) and McDonald (2008). Numerical simulations by Dalal et al. (2008) are in qualitative agreement with the analytical predictions confirming the presence of a scale-dependent bias. Using these analytical models for halo biasing to describe the clustering amplitude of luminous red galaxies (LRGs) and quasars from the Sloan Digital Sky Survey (SDSS), Slosar et al. (2008) obtained $-29 < f_{\rm NL} < 69$ at the 95 per cent confidence level. This shows that LSS studies are competitive with CMB experiments to constrain primordial non-Gaussianity but also calls for more accurate parametrizations of the mass function and clustering statistics of dark-matter haloes arising from non-Gaussian initial conditions.

Most of the analytic derivations of the non-Gaussian halo mass function (e.g. Matarrese et al. 2000; LoVerde et al 2008) are based on the extended Press–Schechter model (Press & Schechter 1974; Bond et al. 1991) which, in the Gaussian case, is known to produce inaccurate estimates of halo abundance (Sheth & Tormen 1999; Jenkins et al. 2001). Similarly, the scale-dependent bias is obtained either using the peak-background split model (Slosar et al. 2008) or assuming that haloes form from the highest linear density peaks (Matarrese & Verde 2008). Both techniques have limited validity in the Gaussian case (Jing 1998; Porciani, Catelan & Lacey 1999; Sheth & Tormen 1999). In this paper, we test the accuracy of the excursion-set model and the peak-background split in the non-Gaussian case. This extends the previous studies of Kang, Norberg & Silk (2007), Grossi et al. (2007) and Dalal et al. (2008) for the halo mass function and of Dalal et al. (2008) for the halo bias by exploring more realistic values for $f_{\rm NL}$ with simulations of better quality. In practice, we run a series of high-resolution N-body simulations where we follow the process of structure formation starting from Gaussian and non-Gaussian initial conditions. The halo mass function and bias extracted from the simulations are then compared with the existing analytical models and used to build accurate fitting formulae. These will provide a benchmark for future determinations of non-Gaussianity with galaxy surveys.

The paper is organized as follows. In Section 2, we describe our N-body simulations. In Sections 3–5, we present our results for the halo mass function, the matter power spectrum and the halo bias, respectively. In Section 6, we discuss the implications of our results for the analysis by Slosar et al. (2008). Our conclusions are summarized in Section 7.

Table 1. Specifics of the N-body simulations.

Name	$f_{\rm NL}$	$N_{\rm part}$	$L_{\rm box}$ (h^{-1} Mpc)	$M_{\rm part}$ ($h^{-1}\,{\rm M}_\odot$)	$L_{\rm soft}$ (h^{-1} kpc)	$z_{\rm start}$	Cosmology
1.750	+750	1024^3	1200	1.246×10^{11}	20	50	*WMAP*5
1.500	+500	1024^3	1200	1.246×10^{11}	20	50	*WMAP*5
1.250	+250	1024^3	1200	1.246×10^{11}	20	50	*WMAP*5
1.80	+80	1024^3	1200	1.246×10^{11}	20	50	*WMAP*5
1.27	+27	1024^3	1200	1.246×10^{11}	20	50	*WMAP*5
1.0	0	1024^3	1200	1.246×10^{11}	20	50	*WMAP*5
1.-27	-27	1024^3	1200	1.246×10^{11}	20	50	*WMAP*5
1.-80	-80	1024^3	1200	1.246×10^{11}	20	50	*WMAP*5
2.0	0	1024^3	1200	1.072×10^{11}	20	50	*WMAP*3
2.750	+750	1024^3	1200	1.072×10^{11}	20	50	*WMAP*3
3.0	0	1024^3	150	2.433×10^{8}	3	70	*WMAP*5
3.250	+250	1024^3	150	2.433×10^{8}	3	70	*WMAP*5

Table 2. Assumed cosmological parameters.

Name	h	σ_8	$n_{\rm s}$	$\Omega_{\rm m}$	$\Omega_{\rm b}$	Ω_Λ
*WMAP*3	0.73	0.76	0.95	0.24	0.042	0.76
*WMAP*5	0.701	0.817	0.96	0.279	0.0462	0.721

2 *N*-BODY SIMULATIONS

2.1 Specifics of the simulations

We use the lean version of the tree-PM code GADGET-2 (Springel 2005) kindly made available by Volker Springel to follow the formation of cosmic structure in a flat Λ cold dark matter cosmology. We run three different series of simulations (each containing 1024^3 collisionless particles) that differ in the adopted cosmology, box size (and thus force softening length, $L_{\rm soft}$) and initial redshift (details are summarized in Table 1). The assumed cosmological parameters are listed in Table 2. For our series 1 and 3, they coincide with the 5-yr *WMAP* best estimates (Komatsu et al. 2008). The combined 3-yr *WMAP*+LSS results by Spergel et al. (2007) are instead used for series 2.

We produce non-Gaussian initial conditions directly applying equation (1) after having generated the Gaussian random field ϕ with standard Fourier techniques. We consider eight values for the parameter $f_{\rm NL}$: -80, -27, 0, $+27$, $+80$, $+250$, $+500$ and $+750$. The first five are within the current constraints from CMB data (Komatsu et al. 2008), while the three largest values are useful to compare with previous work. Within each series of simulations, we use the same set of random phases to generate the Gaussian potential ϕ. This facilitates the comparison between different runs by minimizing sample variance.

The linear matter transfer function, $T(k)$, is computed using the LINGER code (Bertschinger 2001) and is applied after creating the non-Gaussian potential Φ in equation (1). Particle displacements and velocities at $z_{\rm start}$ are generated using the Zel'dovich approximation (Zel'dovich 1970). A critical discussion of this choice is presented in the Appendix.

Particle positions and velocities are saved for 30 time-steps logarithmically spaced in $(1+z)^{-1}$ between $z = 10$ and 0. Dark-matter haloes are identified using the standard friends-of-friends (FOF) algorithm with a linking length equal to 0.2 times the mean inter-particle distance. We only considered haloes containing at least 100 particles.

Our first two series of simulations only include large periodic boxes covering a volume of $(1200\,h^{-1}\,{\rm Mpc})^3$ where we can study haloes with masses ranging from 10^{13} up to $10^{15}\,h^{-1}\,{\rm M}_\odot$. These simulations will be used to analyse both the mass function and the bias of dark-matter haloes. On the other hand, the third series includes simulations covering a volume of $(150\,h^{-1}\,{\rm Mpc})^3$. They will be used to study the mass function and the bias of low-mass haloes with $10^{10} < M < 10^{13}\,h^{-1}\,{\rm M}_\odot$.

2.2 A note on the definition of $f_{\rm NL}$

The definition of $f_{\rm NL}$ given in equation (1) depends on the cosmic epoch at which it is applied. The reason for this time dependence is that both potentials Φ and ϕ decay with time proportionally to $g(a) = D(a)/a$ with $D(a)$ the linear growth factor of density fluctuations and a the Robertson–Walker scale factor.

In this paper, we define $f_{\rm NL}$ by applying equation (1) at early times, namely at $z = \infty$. Other authors have adopted different conventions. Grossi et al. (2007) use the linearly extrapolated fields at $z = 0$ to define $f_{\rm NL}$. Therefore, their values of the $f_{\rm NL}$ parameter need to be divided by the factor $g(\infty)/g(0)$ to match ours. In the *WMAP*5 cosmology, $g(\infty)/g(0) \simeq 1.3064$. On the other hand, Dalal et al. (2008) apply equation (1) at $z_{\rm start}$, the redshift at which they generate the initial conditions for the simulations. This agrees with our definition to better than 0.01 per cent.

The sign convention for the non-linearity parameter might possibly generate further ambiguity. In our simulations, positive values $f_{\rm NL}$ correspond to positive skewness of the mass-density probability distribution function. The same convention has been adopted by Grossi et al. (2007), Kang et al. (2007) and Dalal et al. (2008).

3 THE HALO MASS FUNCTION

One of the long-standing efforts in cosmology is to determine the mass function of dark matter haloes ${\rm d}n/{\rm d}M(M, z)$ – i.e. the number of haloes per unit volume per unit mass at redshift z – from the statistical properties of the linear density field. Analytical work has suggested that, when expressed in terms of suitable variables, the functional form of ${\rm d}n/{\rm d}M$ should be universal to changes in redshift and cosmology (Press & Schechter 1974; Bond et al. 1991; Sheth & Tormen 1999). N-body simulations have shown that this is approximately true when structure formation is seeded by Gaussian perturbations (Jenkins et al. 2001; Evrard et al. 2002; White 2002; Warren et al. 2006; Tinker et al. 2008).

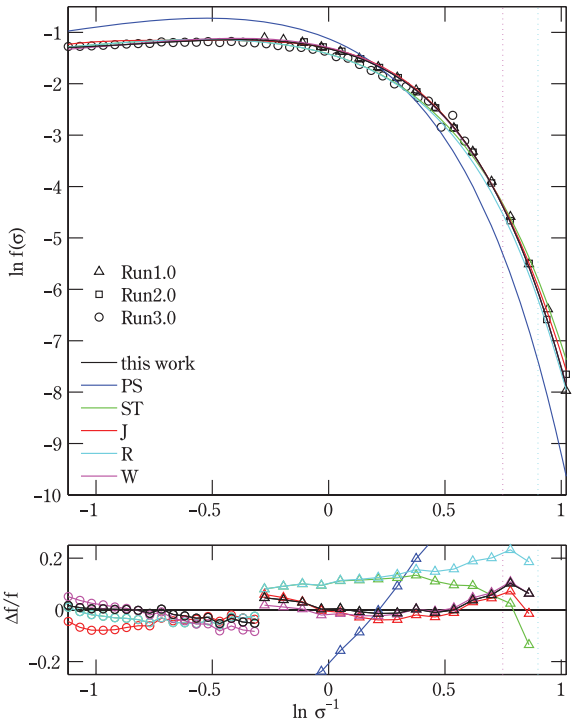

Figure 1. The universal mass function in our Gaussian simulations Run 1.0 (triangles), Run 2.0 (squares) and Run 3.0 (circles) is compared with a number of fitting formulae listed in Table 3. Data are equispaced in $\ln\sigma^{-1}$ and only bins containing more than 30 haloes are shown. The vertical dotted lines indicate the upper mass limits used in Jenkins et al. (2001), Reed et al. (2003), and Warren et al. (2006). The corresponding low-mass limits are all equal or smaller than $\ln\sigma^{-1} = -1.2$. The lower panel shows the residuals $\Delta f/f =$ [(data − fit)/data] between our data points and the different fitting functions. Here, we only show data with a Poisson uncertainty better than 5 per cent. For clarity only outputs from Run 1.0 (triangles, $\ln\sigma^{-1} > -0.3$) and Run 3.0 (circles, $\ln\sigma^{-1} < -0.3$) are plotted.

Following these studies, we describe the halo abundance in our simulations through the following functional form

$$\frac{\mathrm{d}n}{\mathrm{d}M}(M,z) = f(\sigma)\,\frac{\bar{\rho}_\mathrm{m}}{M}\,\frac{\mathrm{d}\ln[\sigma^{-1}(M,z)]}{dM}\,. \qquad (2)$$

where $\bar{\rho}_\mathrm{m}$ is the mean background matter density today, and $\sigma^2(M, z)$ is the variance of the linear density field

$$\sigma^2(M,z) = \frac{1}{2\pi^2}\int_0^\infty k^2\,P_\mathrm{lin}(k,z)\,W^2(k,M)\,\mathrm{d}k, \qquad (3)$$

with $P_\mathrm{lin}(k, z)$ the corresponding power spectrum and $W^2(k, M)$ some window function with mass resolution M (here top-hat in real space). The validity of equation (2) has been widely tested against numerical simulations and useful parametrizations for $f(\sigma)$ have been provided starting from Gaussian initial conditions (Sheth & Tormen 1999; Jenkins et al. 2001; Warren et al. 2006). These fitting functions have an accuracy ranging from 5 to 20 per cent depending on redshift, cosmology and the exact definition of halo masses. Recently, Tinker et al. (2008) have detected deviations from universality in $f(\sigma)$: redshift-dependent corrections are needed to match the mass function in simulations with an accuracy of 5 per cent. This result is based on haloes identified with the spherical overdensity algorithm. It is well known that the mass function of FOF haloes shows a more universal scaling even though other halo finders might be more directly linked to actual observables (Jenkins et al. 2001; Tinker et al. 2008). Deviations from universality for FOF haloes will be further discussed in Section 3.3. One should anyway keep in mind that baryonic physics can cause 30 per cent deviations in $\mathrm{d}n/\mathrm{d}M$ with respect to the pure dark-matter case (Stanek, Rudd & Evrard 2008).

3.1 Halo mass function from Gaussian initial conditions

The halo mass functions extracted from our Gaussian simulations – Run 1.0 (triangles), Run 2.0 (squares) and Run 3.0 (circles) – are presented in Fig. 1. The combination of different box sizes allows us to cover the very wide range $-1.2 < \ln\sigma^{-1} < 1.1$ which roughly corresponds to the mass interval $2\times10^{10} < M < 5\times10^{15}\,h^{-1}\,\mathrm{M}_\odot$ at $z = 0$. Fig. 1 has been obtained by combining data from snapshots at redshifts $z < 1.6$. Note that, at a fixed redshift, larger values of σ^{-1} correspond to higher masses. On the other hand, with increasing the redshift, larger values of σ^{-1} are associated with a given halo mass. Even though data points correspond to different redshifts and cosmologies, they all form a well-defined sequence. This indicates that the function $f(\sigma)$ is universal to good approximation. For a given σ, outputs at a fixed redshift scatter around the universal sequence by 10–15 per cent. A number of fitting formulae have been proposed in the literature to parametrize this sequence. In Fig. 1, we compare some of them (summarized in Table 3) with our data points. Fractional deviations between models and data are shown in the bottom panel. Barring the classical Press–Schechter result, all the fitting formulae describe our data to better than 20 per cent. The best agreement is found all over the mass range with Warren et al. (2006) followed by Jenkins et al. (2001) which both show deviations from our data at the 10 per cent level. The Sheth & Tormen (1999) model also provides an accurate description of the data for small halo masses, but tends to overestimate the abundance of the most massive objects. On the other hand, the fit by Reed et al. (2003) tends to underestimate the high-mass tail of the mass

Table 3. Widely used parametrizations for the halo mass function deriving from Gaussian initial conditions.

Acronym	Reference	Functional form	Parameters
PS	Press & Schechter (1974)	$f_\mathrm{PS}(\sigma) = \sqrt{\frac{2}{\pi}}\,\frac{\delta_c}{\sigma}\,\exp\left(-\frac{\delta_c^2}{2\sigma^2}\right)$	$\delta_c = 1.686$
ST	Sheth & Tormen (1999)	$f_\mathrm{ST}(\sigma) = A\sqrt{\frac{2a}{\pi}}\,\frac{\delta_c}{\sigma}\exp\left(-\frac{a\,\delta_c^2}{2\sigma^2}\right)\left[1+\left(\frac{\sigma^2}{a\,\delta_c^2}\right)^p\right]$	$A = 0.322$, $a = 0.707$, $p = 0.3$
J	Jenkins et al. (2001)	$f_\mathrm{J}(\sigma) = A\exp\left(-\lvert\ln\sigma^{-1} + B\rvert^p\right)$	$A = 0.315$, $B = 0.61$, $p = 3.8$
R	Reed et al. (2003)	$f_\mathrm{R}(\sigma) = f_\mathrm{ST}(\sigma)\exp\left(\frac{-a}{\sigma(\cosh 2\sigma)^b}\right)$	$a = 0.7$, $b = 5$
W	Warren et al. (2006)	$f_\mathrm{W}(\sigma) = A\left(\sigma^{-a} + b\right)\exp\left(-\frac{c}{\sigma^2}\right)$	A = 0.7234, a = 1.625, b = 0.2538, c = 1.1982
T	Tinker et al. (2008)	$f_\mathrm{T}(\sigma) = A\left[\left(\frac{\sigma}{b}\right)^{-a} + 1\right]\exp\left(-\frac{c}{\sigma^2}\right)$	Vary with halo overdensity

function. Overall our findings are in good agreement with Heitmann et al. (2006) and Lukić et al. (2007).

Following Warren et al. (2006) and Tinker et al. (2008), we fit the outcome of the simulations with the function

$$f(\sigma) = \left[\mathrm{D} + \mathrm{B}\left(\frac{1}{\sigma}\right)^{\mathrm{A}}\right] \exp\left(-\frac{\mathrm{C}}{\sigma^2}\right) . \quad (4)$$

The best-fitting parameters have been determined through χ^2 minimization using the Markov Chain Monte Carlo method, and read

$$\begin{aligned} \mathrm{A} &= 1.868 \pm 0.019, \\ \mathrm{B} &= 0.6853 \pm 0.0035, \\ \mathrm{C} &= 1.2266 \pm 0.0049, \\ \mathrm{D} &= 0.2279 \pm 0.0022 . \end{aligned} \quad (5)$$

In terms of the parametrization given in Warren et al. (2006) and reported in Table 3, this corresponds to (A, a, b, c) = (0.6853, 1.868, 0.3324, 1.2266). The fit in equation (5) describes our data set up to deviations of a few per cent over the entire mass and redshift ranges for Run 1.0 and Run 2.0, while it shows larger deviations (up to nearly 10 per cent) towards the high-mass end of Run 3.0, (see Fig. 1). It is important to remember, however, that Run 3.0 covers a much smaller volume than the others and thus is more severely affected by sample variance.

3.2 The universal halo mass function from non-Gaussian initial conditions

Is the function $f(\sigma^{-1})$ universal also in the non-Gaussian case? This question is addressed in Fig. 2, where we show the output of our main series of simulations at four redshifts ($z = 0$, 0.5, 1, 1.6) to test the scaling of the mass function in terms of σ^{-1}. Only bins containing at least 20 haloes are considered. Within a certain tolerance, the halo mass functions at different masses and redshifts all lie on the same curve for a given $f_{\rm NL}$. The scatter of the points at a fixed redshift around this curve roughly amounts to 10 per cent, and it becomes smaller towards our largest values of $f_{\rm NL}$.

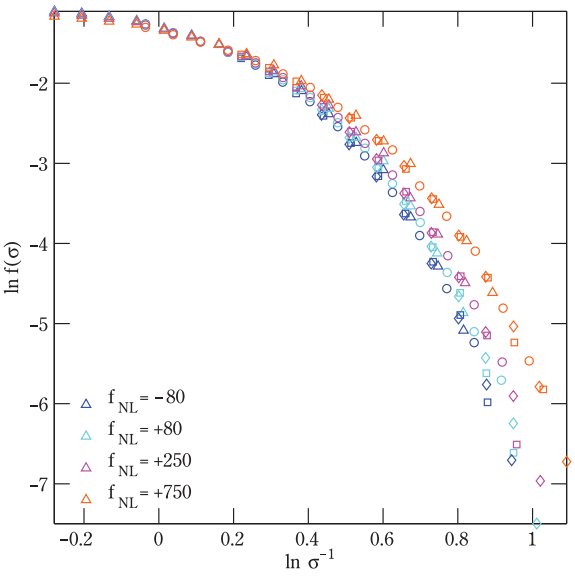

Figure 2. Universality of the mass function arising from non-Gaussian initial conditions. Colours refer to simulations with different values of $f_{\rm NL}$ as indicated by the labels. Symbols identify the redshift of the simulation output from which the mass function has been calculated, namely $z = 0$ (triangles), 0.5 (circles), 1 (squares) and 1.6 (diamonds).

We thus generalize equation (2) to non-Gaussian initial conditions by assuming that

$$\frac{\mathrm{d}n}{\mathrm{d}M}(f_{\rm NL}, M, z) = f(f_{\rm NL}, \sigma)\,\frac{\bar{\rho}_{\rm m}}{M}\,\frac{\mathrm{d}\ln[\sigma^{-1}(M,z)]}{\mathrm{d}M} , \quad (6)$$

and we provide a fitting formula for $f(f_{\rm NL}, \sigma)$. Given the similarity to the Gaussian case, we still adopt the functional form given in equation (4) but let the parameters A, B, C, D vary with $f_{\rm NL}$. The best-fitting values have been determined in two steps. We first used a Markov Chain Monte Carlo method to determine A, B, C, D at fixed $f_{\rm NL}$ through χ^2 minimization. The results suggest that the $f_{\rm NL}$ dependence for each parameter of the mass function can be accurately described by polynomials of different orders. Eventually, we used the data to derive the coefficients of these polynomials.

The degree of complexity required to fit the simulation data grows considerably with increasing $f_{\rm NL}$. For $-80 \le f_{\rm NL} \le 250$ (a range that fully encloses the values currently allowed by CMB studies), the mass-function parameters in equation (4) are well approximated by the linear relation

$$\mathrm{P}(f_{\rm NL}) = \mathrm{p}_1 + \mathrm{p}_2 f_{\rm NL}, \quad \text{for P} = \mathrm{A, B, C, D}. \quad (7)$$

Table 4 lists the corresponding best-fitting parameters. The quality of this fitting formula is assessed in the left-hand panel of Fig. 3, where the mass function for the simulations with $f_{\rm NL} = -80$, -27, 0, $+27$, $+80$ and $+250$ is compared with the corresponding fit. Residuals (shown in the bottom panel) are smaller than 5 per cent all over the range $-0.2 < \ln\sigma^{-1} < 0.8$ corresponding to the mass interval $2 \times 10^{13} < M < 2 \times 10^{15}\,h^{-1}\,\mathrm{M}_\odot$ at $z = 0$.

On the other hand, equation (7) is not suitable to account for values of $f_{\rm NL}$ substantially larger than 250. To obtain an accurate fit of the universal halo mass function over the range $-80 \le f_{\rm NL} \le 750$, we had to consider polynomials up to fourth order in $f_{\rm NL}$,

$$\mathrm{P}(f_{\rm NL}) = \mathrm{p}_1 + \mathrm{p}_2 f_{\rm NL} + \mathrm{p}_3 f_{\rm NL}^2, \quad \text{for P} = \mathrm{A, C} \quad (8)$$

and

$$\mathrm{P}(f_{\rm NL}) = \mathrm{p}_1 + \mathrm{p}_2 f_{\rm NL} + \mathrm{p}_3 f_{\rm NL}^2 + \mathrm{p}_4 f_{\rm NL}^3 + \mathrm{p}_5 f_{\rm NL}^4, \quad \text{for P} = \mathrm{B, D}. \quad (9)$$

The best-fitting values of the parameters above are listed in Table 5 while the corresponding functions are compared with the simulation data in the right-hand panel of Fig. 3. Also in this case residuals are smaller than 5 per cent for $\ln\sigma^{-1} < 0.8$.

The universality of the fitting formula in equation (6) has been further tested against our non-Gaussian simulation of the *WMAP*3 cosmology, Run2.750, which has not been used to determine the best-fitting parameters. This blind check shows that, in the range $-0.27 < \ln\sigma^{-1} < 0.94$ (roughly corresponding to $1.6 \times 10^{13} < M < 2.2 \times 10^{15}\,h^{-1}\,\mathrm{M}_\odot$ at $z = 0$), the provided fit reproduces the mass function with an accuracy of 5 per cent.

We warn the readers against extending our fitting formulae beyond their range of validity, in particular at low halo masses. The simulations of our main series resolve $10^{13}\,h^{-1}\,\mathrm{M}_\odot$ haloes with 100 particles. For $f_{\rm NL} \neq 0$, our analytical formulae for the mass function have been derived using only haloes that are more massive than this limit. Moreover, since the high-mass tail of the mass function is enhanced (suppressed) for positive (negative) values of $f_{\rm NL}$ with respect to the Gaussian case, mass conservation requires that the opposite effect is seen at lower masses. We have directly tested the goodness of our fit towards the smaller masses using Run3.250 (which has a box size 8 times smaller than for the simulations in the

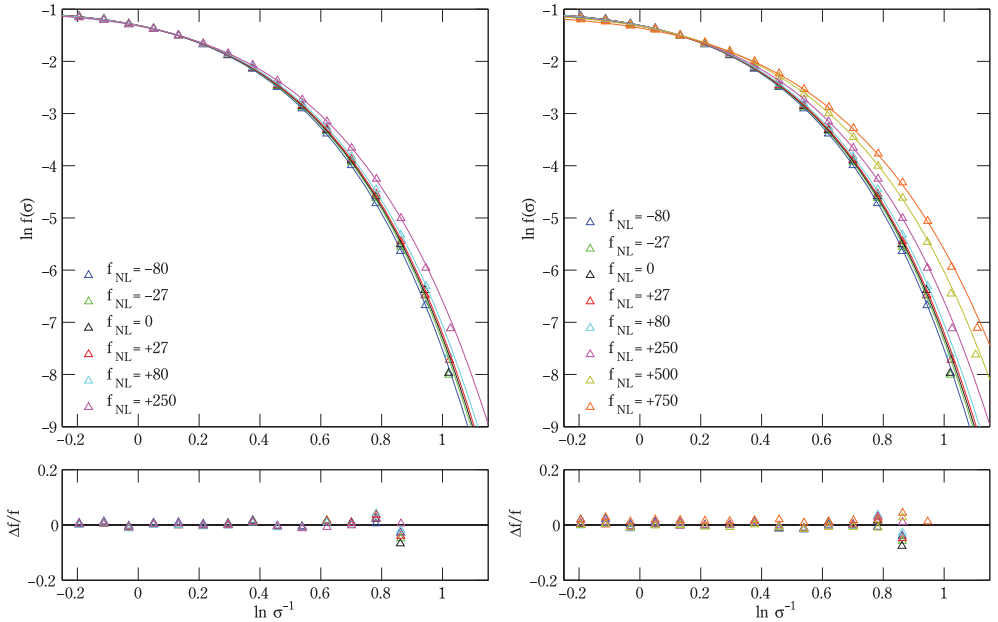

Figure 3. Comparison between the halo mass function from our main series of simulations (triangles) and the corresponding fitting functions (lines). Values $-80 \leq f_{\rm NL} \leq 250$ and the fit in equation (7) are considered in the left-hand panel. All the simulations and the polynomial fit in equations (8) and (9) are shown in the right-hand panel. The lower panels show residuals $\Delta f/f = [(\text{data} - \text{fit})/\text{data}]$ for data points with a statistical uncertainty which is smaller than 5 per cent.

Table 4. Best-fitting values for the linear coefficients of the universal mass-function parameters given in equation (7). The quoted values are truncated at the first digit which is affected by the statistical errors. This provides an accurate description of our simulations for $-80 \leq f_{\rm NL} \leq 250$.

Parameter	p_1	p_2
A	1.694	−0.00199
B	0.566	−0.00029
C	1.151	−0.00071
D	0.287	−0.00030

main series but the same number of particles) and indeed found that the fitting formulae in equations (8) and (9) systematically overestimate the abundance of small mass haloes by 10–30 per cent. We will address the low-mass tail of the mass function for $f_{\rm NL} \neq 0$ in future work.

On the other hand, for Gaussian initial conditions, we combined simulations with different box sizes to derive the fitting function in equations (4) and (5). This allowed us to extend the validity of our fit to the much wider mass range $2.4 \times 10^{10} < M < 5 \times 10^{15}\, h^{-1}\,{\rm M}_\odot$.

Our fitting formulae give three different approximations for the universal mass function in the Gaussian case. In general, the fit given in equations (4) and (5) has to be preferred as it has been obtained from a richer data set spanning a much wider range of halo masses. However, for masses above $10^{13}\, h^{-1}\,{\rm M}_\odot$ at $z = 0$, the fit in equations (4) and (7) and Table 4 provides the most accurate representation of our data. In any case, the different fitting functions never deviate by more than 3–4 per cent. Also note that our two fitting functions for the non-Gaussian simulations agree by better than 1 per cent for $-27 \leq f_{\rm NL} \leq 80$ and by a few per cent for $f_{\rm NL} = -80$ and $+250$.

3.3 The limit of universality: redshift dependence

Regardless of the value of $f_{\rm NL}$, we have found that the halo mass function is universal, when written in terms of σ^{-1}, with an accuracy of roughly 10 per cent. If one is interested in giving analytical approximations for the halo mass function which are more accurate than the universal fit, it is necessary to introduce redshift-dependent corrections (see also Tinker et al. 2008 for the Gaussian case). In the left-hand panel of Fig. 4, we show how well the universal fit (whose parameters are listed in Table 5) describes the simulation outputs at $z = 0$, 0.5, 1 and 1.61. At $z = 0$ and for masses $M \geq 4$–$5 \cdot 10^{14}\,{\rm M}_\odot$, the fitting formula deviates for the data by more than 10 per cent. The smaller the redshift, the worse is the agreement between the data points and the universal fit. The bigger the $f_{\rm NL}$, the less critical is the comparison.

In this section, we provide a non-universal fit which is very accurate at low redshift. In particular, we write

$$\frac{{\rm d}n}{{\rm d}M}(f_{\rm NL}, M, z) = f(f_{\rm NL}, \sigma_0, z)\, \frac{\bar{\rho}_{\rm m}}{M} \frac{{\rm d}\ln[\sigma_0^{-1}(M)]}{{\rm d}M}\,, \qquad (10)$$

where $\sigma_0 = \sigma(z = 0) = \sigma(z)/D_+(z)$ is the rms deviation of the linear density field at $z = 0$. We approximate f with the functional form given in equation (4) but now let the parameters A, B, C, D vary with both $f_{\rm NL}$ and z. Markov Chain Monte Carlo fitting suggests that each parameter A, B, C, D of the mass function can be accurately described as follows:

$$\mathrm{P}(z,\, f_{\rm NL}) = \mathrm{p}_1\,[1 + \mathrm{p}_2 z + \mathrm{p}_3 z^2]\,[1 + \mathrm{p}_4 f_{\rm NL}]\,. \qquad (11)$$

The best-fitting parameters for $-80 \leq f_{\rm NL} \leq 80$ and $0 \leq z \leq 0.5$ are listed inTable 6, while the quality of the fitting formula is assessed in the right-hand panel of Fig. 4. Residuals are smaller than 5 per cent all over the mass range, indicating that for $-80 \leq f_{\rm NL} \leq 80$ and $0 \leq z \leq 0.5$ the fit of equations (10), (4) and (11) has to be preferred to the universal fit given in the previous section. On the other hand, for higher values of $|f_{\rm NL}|$ and for higher redshifts,

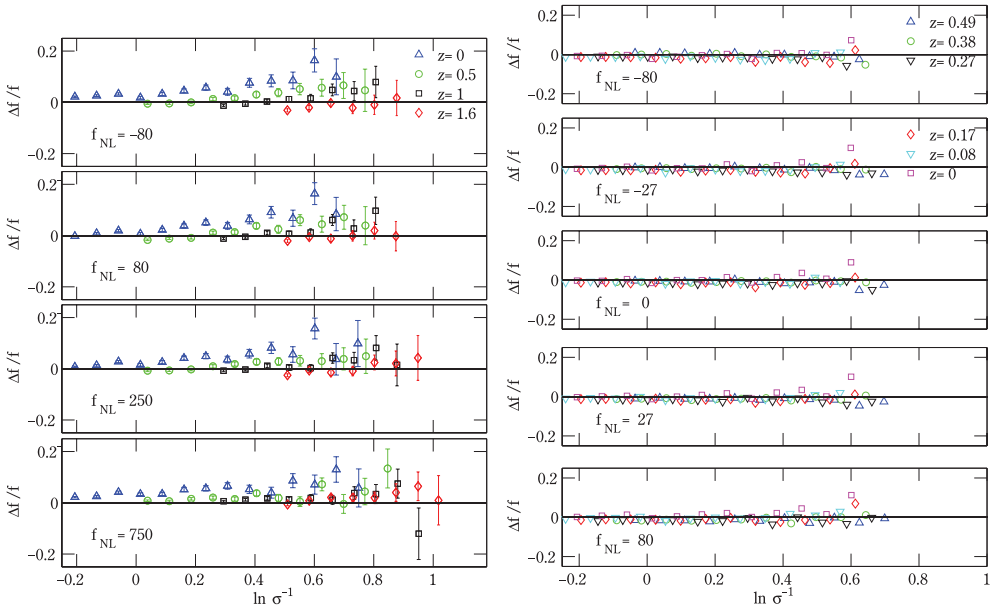

Figure 4. Left-hand panel: mass function residuals of Run1.−80, Run1.80, Run1.250, Run1.750 with respect to the universal fit given in equations (8) and (9) at redshift $z = 0$, 0.5, 1, 1.61 (indicated by the symbols and colours). Only data points with a statistical error smaller than 10 per cent are shown. Right-hand panel: as in the left-hand panel but for the non-universal fit given in equation (11). In this case, only data points with an accuracy better than 5 per cent are shown.

Table 5. As in Table 4 but for the fitting formula in equations (8) and (9). This accurately describes the mass function in all our non-Gaussian simulations ($-80 \leq f_{\rm NL} \leq 750$).

Parameter	p_1	p_2 (10^{-3})	p_3 (10^{-7})	p_4 (10^{-9})	p_5 (10^{-12})
A	1.708	−2.07	3.1	0	0
B	0.560	−0.46	+12.46	−2.36	+2.65
C	1.150	−0.76	+2.7	0	0
D	0.293	−0.16	−14.07	+3.88	−3.94

Table 6. Best-fitting values for the mass-function parameters given in equation (11). This provides an accurate description of the data for $0 \leq z \leq 0.5$ and $-80 \leq f_{\rm NL} \leq 80$. The universal function of equations (6), (4), (8) and (9) should be used otherwise.

Parameter	p_1	p_2 (10^{-1})	p_3 (10^{-1})	p_4 (10^{-4})
A	1.82	2.85	4.53	−5.92
B	0.578	5.30	7.53	−7.73
C	1.15	9.52	9.08	−4.42
D	0.294	4.92	4.67	−3.80

the universal fit gives a better and more economic (in terms of parameters) description of the data.

3.4 Comparison with theoretical models

The halo mass function arising from mildly non-Gaussian initial conditions can be modelled by generalizing the Press–Schechter formalism. Using the saddle-point approximation to evaluate the probability for the linear density field to be above a given threshold value, Matarrese et al. (2000) have derived a model for $\mathrm{d}n/\mathrm{d}M$. More recently, LoVerde et al (2008) presented another expression for the mass function by using the Edgeworth asymptotic expansion for the probability density function of the linear density field. In both cases, only leading-order corrections in $f_{\rm NL}$ have been accounted for. In absolute terms, these models are not expected to be accurate as they should suffer from the same shortcomings as the Press–Schechter model in the Gaussian case. However, they can be used to compute the fractional non-Gaussian correction $f(M, z, f_{\rm NL})/f(M, z, f_{\rm NL} = 0)$ (Verde et al. 2000; LoVerde et al 2008). In Fig. 5, we use this quantity to test the models against our simulations. Data points with errorbars show the N-body output at $z = 0$, 0.5 and 1, while the dotted lines indicate the models of Matarrese et al. (2000) and LoVerde et al (2008) as indicated in equations (B.6)[1] and (4.19) of LoVerde et al (2008), respectively. It is evident that the models overestimate the non-Gaussian correction. Following the indications in Carbone et al. (2008), we also show a modified version of the models which is obtained by lowering the critical threshold for halo collapse as $\delta_{\rm c} \simeq 1.5$ (solid lines in Fig. 5). Such a correction vastly improves the agreement with the simulations.

Dalal et al. (2008) proposed to fit the halo mass function in terms of the convolution between $\mathrm{d}n/\mathrm{d}M(f_{\rm NL} = 0, M, z)$ and a Gaussian kernel in M with a $f_{\rm NL}$-dependent mean and variance. Fig. 5 shows that their fit tends to overestimate the non-Gaussian corrections especially for large, positive values of $f_{\rm NL}$ and masses $M < 10^{14}\, h^{-1}\, \mathrm{M}_{\odot}$. On the other hand, for $|f_{\rm NL}| < 100$ it has a similar accuracy as the formulae derived from the Press–Schechter formalism corrected with the reduced threshold.

The good agreement between the fractional non-Gaussian corrections derived from the modified PS models and from the simulations is not enough to derive $f_{\rm NL}$ from future observations of galaxy clusters. In fact the ratio $f(z, f_{\rm NL})/f(z, f_{\rm NL} = 0)$ is not an observable: the only quantity that we can hope to compare with observations is the mass function. In order to make predictions for $\mathrm{d}n/\mathrm{d}M$, the models for the fractional non-Gaussian correction need

[1] This fixes a typo in equation (68) of Matarrese et al. (2000).

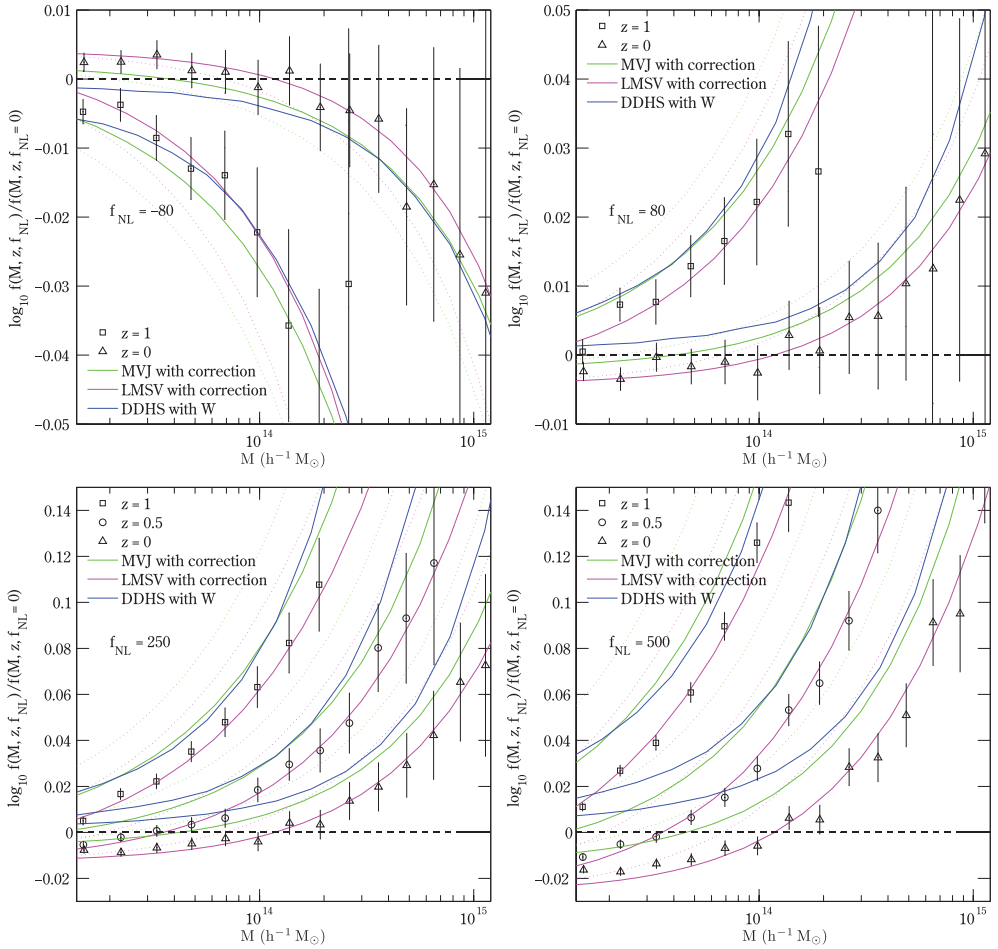

Figure 5. Comparison between the halo mass functions from our simulations and from the models by Matarrese et al. (2000), LoVerde et al (2008) and the fit by Dalal et al. (2008) for different values of $f_{\rm NL}$ (different panels) and for $z = 0$, 0.5, 1 (triangles, circles, squares, respectively). The quantity which is plotted is the ratio $f(z, f_{\rm NL})/f(z, f_{\rm NL} = 0,)$. The dotted lines indicate the models of Matarrese et al. 2000 (green) and LoVerde et al 2008 (magenta), as they appear in equations (B.6) and (4.19) of LoVerde et al (2008), respectively. The corresponding solid lines indicate the same models with a reduced threshold for halo collapse: $\delta_{\rm c} \simeq 1.5$. The blue solid lines are obtained by convolving the $f_{\rm NL}$-dependent kernel given in Dalal et al. (2008) with the mass-function fit for the Gaussian case by Warren et al. (2006).

to be multiplied by a Gaussian mass function. This step might introduce relatively large systematic errors (see Fig. 1) which could degrade any measurement of $f_{\rm NL}$ based on the cluster mass function. We address this issue in Fig. 6 where we plot the fractional deviation of some model predictions for the function f with respect to the simulation output (results are very similar for different values of $f_{\rm NL}$). We consider the model by LoVerde et al (2008) corrected with the factor $\mathcal{N}$ and multiplied by three different Gaussian models: Sheth & Tormen (1999), Warren et al. (2006) and our fit with $f_{\rm NL} = 0$. Note that some of the final outcomes systematically differ by 10–20 per cent over the entire mass range covered by the simulations. This clearly shows that a careful measurement of the Gaussian mass function is necessary to avoid a biased estimation of the non-linearity parameter. Note that, for $|f_{\rm NL}| < 100$, the models by Matarrese et al. (2000) and LoVerde et al (2008) (both with the reduced collapse threshold) combined with our Gaussian fit are in rather good agreement with the numerical mass functions (similar results are obtained using the Gaussian fit by Warren et al. (2006) for masses below a few $\times\, 10^{14}\, h^{-1}\, {\rm M}_\odot$). Perhaps not surprisingly, no model describes the simulation data for all the values of $f_{\rm NL}$ as well as our fitting formulae for the non-Gaussian mass function given in Sections 3.2 and 3.3.

3.5 Summary of accuracy and range of validity of the mass function fits

In order to facilitate the use of our fitting formulae for the halo mass function, we summarize here their accuracy and range of validity.

(i) For $-80 \le f_{\rm NL} \le 80$ and $0 \le z \le 0.5$, the best description (with 5 per cent accuracy) of our numerical data is given by equations (10), (4) and (11).

(ii) For larger values of $f_{\rm NL}$ and z (but with $f_{\rm NL} \le 750$ and $z \le 1.6$) or whenever an accuracy of 10 per cent is enough, the universal fits of Section 3.2 should be used:

(iii) universal fit for $-80 \le f_{\rm NL} \le 250$: equations (4), (7) and Table 4;

(iv) universal fit for $-80 \le f_{\rm NL} \le 750$: equations (4), (8), (9) and Table 5.

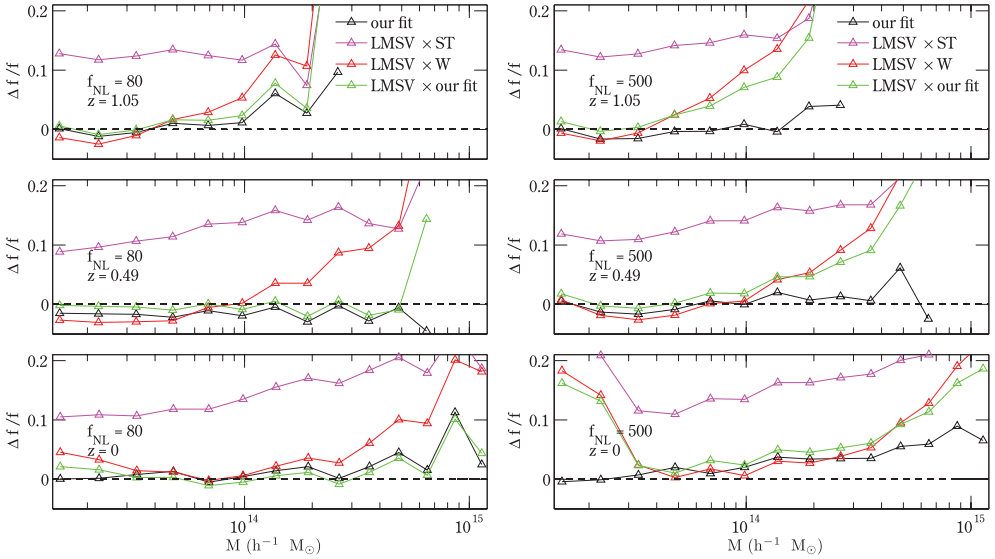

Figure 6. Residuals between the simulated mass functions and various model prescriptions, for Run1.80 (left-hand panels) and Run1.500 (right-hand panel) at $z = 0$, 0.5, 1. The models have been obtained multiplying the formula for $f(z, f_{\rm NL})/f(z, f_{\rm NL} = 0,)$ by LoVerde et al (2008) (with the reduced $\delta_{\rm c}$ as the solid lines in Fig. 5) with different Gaussian mass functions: Sheth & Tormen 1999 (magenta), Warren et al. 2006 (red) and our Gaussian fit (green). The black lines show residuals with respect to our fitting formula given in Sections 3.2 and 3.3. Only data with errors smaller than 10 per cent are shown.

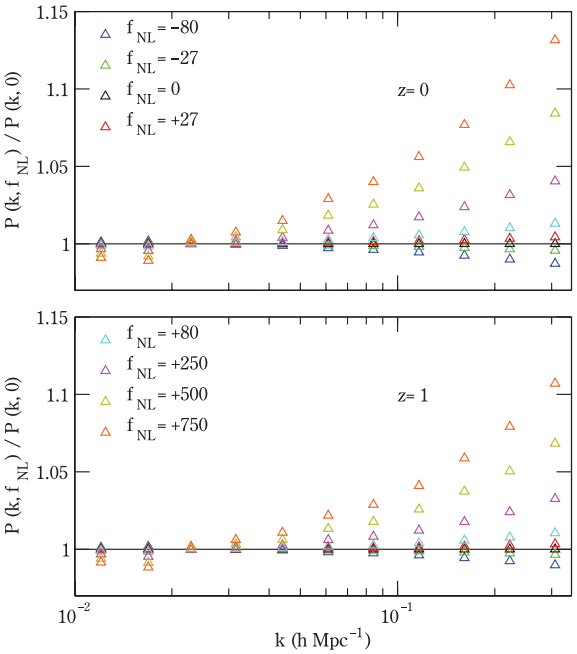

Figure 7. Ratio between the matter power spectra of non-Gaussian and Gaussian simulations at redshift $z = 1$ (bottom) and $z = 0$ (top). Data are extracted from the N-body simulations in our main series where identical random phases have been used to generate ϕ for all values of $f_{\rm NL}$.

4 MATTER POWER SPECTRUM

In this section, we study how non-Gaussian initial conditions influence the power spectrum of the mass density field. At tree level, the power spectrum does not depend on $f_{\rm NL}$ in Eulerian perturbation theory. However, one-loop corrections make the power spectrum $f_{\rm NL}$-dependent. Qualitatively, theoretical expectations are that positive (negative) values of $f_{\rm NL}$ tend to enhance (suppress) the amplitude of the power spectrum on non-linear scales. In Fig. 7, we plot the ratio of power spectra $P(k, f_{\rm NL})/P(k, f_{\rm NL} = 0)$ extracted from the simulations of our main series at redshifts $z = 0$ and 1. The matter power spectrum of non-Gaussian models appears to deviate already by a few per cent at $k = 0.1\,h\,{\rm Mpc}^{-1}$. As expected, deviations become more severe with increasing the wavenumber k. Our results are in agreement with the perturbative calculations by Taruya, Koyama & Matsubara (2008). We note, however, that Grossi et al. (2008) found smaller deviations between the non-Gaussian and Gaussian power spectra at larger values of k and $f_{\rm NL}$.

Our results have two important practical implications. First, the widespread habit of using the Gaussian matter power spectrum to determine non-Gaussian bias parameters leads to scale-dependent systematic errors that might become severe when high-precision is required. Secondly, primordial non-Gaussianity modifies the power-spectrum on the scales where baryonic oscillations (BAOs) are present. Reversing the argument, two-point statistics could be also used to constrain the value of $f_{\rm NL}$. Note, however, that all probes based on galaxy clustering will suffer from uncertainties in the bias parameter (and its scale dependence) that might hinder a measure of $f_{\rm NL}$ based on the study of BAOs. On the other hand, weak lensing studies will directly measure the matter power spectrum. The target of many future wide-field missions is to provide estimates at the per cent level. For parameter estimation, a comparable accuracy will be required on model spectra within a wide range of wavenumbers centred around $k \sim 1\,h\,{\rm Mpc}^{-1}$ (Huterer & Takada 2005). Therefore, even values of $f_{\rm NL}$ within the current CMB constraints could imprint detectable effects in the matter power spectrum at the scales of interest. The key question is whether one can discern the effect of $f_{\rm NL}$ and, consequently, how much primordial non-Gaussianity will affect the estimate of the other cosmological parameters. We will get back to this in future work.

5 HALO CLUSTERING

The clustering of dark-matter haloes is biased relative to that of the underlying mass distribution by an amount which depends on halo mass, redshift, and the scale at which the clustering is considered

(see e.g. Mo & White 1996; Catelan et al. 1998; Smith, Scoccimarro & Sheth 2007). For Gaussian initial conditions, this has been widely tested against numerical simulations (e.g. Sheth, Mo & Tormen 2001; Seljak & Warren 2004; Tinker et al. 2005).

In general, the halo bias can be quantified using either the power spectrum of the halo density field, $P_{\rm hh}$, or the cross-spectrum between the halo and the underlying matter density field, $P_{\rm hm}$. In the two cases, the bias reads

$$b_{\rm hh}(k, M, z) = \sqrt{\frac{P_{\rm hh}(k, M, z)}{P(k, z)}} \qquad (12)$$

or

$$b_{\rm hm}(k, M, z) = \frac{P_{\rm hm}(k, M, z)}{P(k, z)}\ , \qquad (13)$$

where $P(k, z)$ is the matter power spectrum. If the bias due to halo formation is local and deterministic then $b_{\rm hh} = b_{\rm hm}$ apart from measurement errors. However, in the presence of a stochastic component that does not correlate with the density field $b_{\rm hh} \geq b_{\rm hm}$. In practice, however, the measurement of all power spectra is affected to some level by shot noise due to the discrete nature of dark-matter haloes and N-body particles. If the distribution of the tracers can be approximated as the Poisson sampling of an ideal density field, then the measured power spectrum corresponds to that of the underlying field plus the mean volume per particle (Peebles 1980). Discreteness effects are thus expected to be negligible for P and $P_{\rm hm}$ due to the large number density of particles in the simulations. On the other hand, massive haloes are rare and, being extended objects, cannot be modelled as the Poisson sampling of a continuous distribution (Mo & White 1996, Magliocchetti & Porciani 2003, Porciani in preparation). It is not clear then how to correct for the discreteness effect in their power spectrum (Smith et al. 2009). For these reasons, we use $b_{\rm hm}$ in our analysis and we adopt $b_{\rm hh}$ (without performing any discreteness correction) only to verify the results (see Fig. 8).

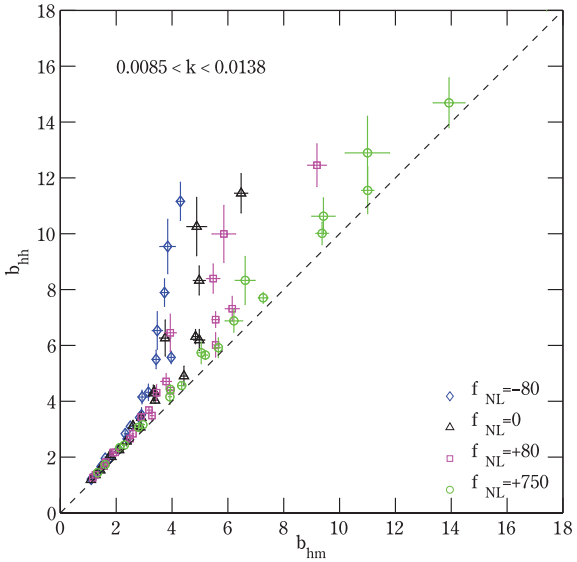

Figure 8. The halo bias from the halo–halo power spectrum (with no discreteness corrections) is plotted against the halo bias from the halo-matter cross-spectrum. Whenever the density of haloes is high enough, the two estimates are very close showing that little stochasticity between mass and halo overdensities is present on the scales of interest (indicated in h Mpc^{-1} in the label). The excess in $b_{\rm hh}$ for rare, massive haloes is likely due to shot noise. Note that large positive values of $f_{\rm NL}$ correspond to more massive haloes and thus allow more accurate measures of high bias parameters.

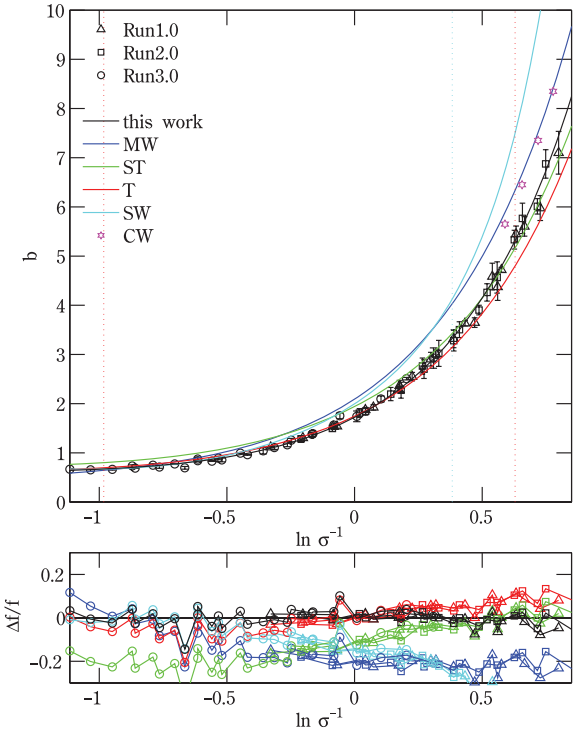

Figure 9. Linear halo bias from the Gaussian simulations Run 1.0 (triangles), Run 2.0 (squares) and Run 3.0 (circles), as a function of σ^{-1}. Only bins containing more than 1000 haloes are shown. The solid lines correspond to the functions listed in Table 7 as indicated by the labels. The four hexagons correspond to the data at $z = 10$ by Cohn & White (2008). The vertical dotted lines indicate the maximum and minimum σ^{-1} considered by Tinker et al. (2005) (red) and Seljak & Warren (2004) (cyan, in this case the minimum σ^{-1} coincides with the frame of the figure).

5.1 Halo bias from Gaussian initial conditions

It is well known that the halo bias factor from Gaussian initial conditions is approximately scale independent for small values of the wavenumber k. We will refer to this asymptotic value on large scales as the 'linear bias' and denote it by b_0. Similarly to the halo mass function, when expressed in terms of σ^{-1}, the linear bias assumes a universal form which, within a given accuracy, is independent of redshift and just weakly dependent on cosmology (e.g. Sheth & Tormen 1999; Seljak & Warren 2004).

We measure the linear bias for the haloes in our simulations as follows. We first determine the functions $b_{\rm hh}$ and $b_{\rm hm}$ by directly applying equations (12) and (13). Within the statistical uncertainties, both functions approach asymptotically to a constant on large scales ($k < 0.05\,h$ Mpc^{-1}). We use the average of the bias function measured in the range $0.01 < k < 0.05\,h$ Mpc^{-1} (4 k-bins) as our estimate of the linear bias. The standard error of the mean is used to quantify the corresponding statistical uncertainty.[2]

In Fig. 9, we show the linear bias obtained from Run 1.0 (triangles), Run 2.0 (squares) and Run 3.0 (circles) as a function of σ^{-1}. Simulation data from snapshots between $z = 0$ and 2 are compared with the commonly used parametrizations listed in Table 7. Our results are in good agreement with the fit by Sheth et al. (2001) for large masses and with that by Tinker et al. (2005) for smaller

[2] Consistently, in what follows, we use the rms value as the error on $b(k, M, z, f_{\rm NL} = 0)$. For $f_{\rm NL} \neq 0$, we assume that the relative error is the same as in the Gaussian case.

Table 7. Commonly used parametrizations for the linear bias arising from Gaussian initial conditions.

Acronym	Reference	Functional form	Parameters and Variables
MW	Mo & White (1996)	$b_{\rm MW} = 1 + \frac{\delta_{\rm c}}{\sigma^2} - \frac{1}{\delta_{\rm c}}$	$\delta_{\rm c} = 1.686$
ST	Sheth et al. (2001)	$b_{\rm ST} = 1 + \frac{1}{\sqrt{a}\delta_{\rm c}}\left[\sqrt{a}\left(a\frac{\delta_{\rm c}^2}{\sigma^2}\right) + \sqrt{a}b\left(a\frac{\delta_{\rm c}^2}{\sigma^2}\right)^{1-c} - \right.$	$\delta_{\rm c} = 1.686$
		$\left. - \frac{\left(a\frac{\delta_{\rm c}^2}{\sigma^2}\right)^c}{\left(a\frac{\delta_{\rm c}^2}{\sigma^2}\right)^c + b(1-c)(1-c/2)}\right]$	$a = 0.707, b = 0.5, c = 0.6$
SW	Seljak & Warren (2004)	$b_{\rm SW} = 0.53 + 0.39(x^{0.45}) + \frac{0.13}{(40x+1)} + 5\times10^{-4}x^{1.5}$	$x = \frac{M}{M_\star}$ with $\sigma(M_*) = 1.686$
T	Tinker et al. (2005)	$b_{\rm T} = b_{\rm ST}$	$\delta_{\rm c} = 1.686, a = 0.707, b = 0.35, c = 0.80$

masses. Note that by combining simulation boxes we are able to explore a larger interval of σ^{-1} than previous studies.

Given that no existing model for the linear bias accurately reproduces our results over the entire mass range spanned by the simulations, we decided to derive a new fitting formula. In particular, we parametrized the outcome of our simulations as

$$b_0 = B_0 + B_1\,\sigma^{-1} + B_2\,\sigma^{-2}\,, \tag{14}$$

and used χ^2 minimization to find

$$\begin{aligned} B_0 &= 0.647 \pm 0.010, \\ B_1 &= -0.540 \pm 0.028, \\ B_2 &= 1.614 \pm 0.019\,. \end{aligned} \tag{15}$$

This fit (which reproduces the numerical data with great accuracy in the range $-1.1 < \ln\sigma^{-1} < 0.8$) should be considered as the linear bias naturally associated with the mass function given in equations (4) and (5).

5.2 Halo bias from non-Gaussian initial conditions

Recent analytical models have suggested that the halo bias arising from non-Gaussian initial conditions of the local type does not tend to a constant on large scales. Rather, the deviation from the Gaussian case should follow

$$\begin{aligned} \Delta b &= b(k, M, z, f_{\rm NL}) - b(k, M, z, f_{\rm NL} = 0) = \\ &= 3\,f_{\rm NL}\,[b_0(M, z) - 1]\,\frac{\delta_{\rm c}}{D(z)}\,\frac{g(\infty)}{g(0)}\,\frac{H_0^2}{c^2}\,\frac{\Omega_{\rm m}}{k^2\,T(k)}\,, \end{aligned} \tag{16}$$

where $\delta_{\rm c} = 1.686$, $c/H_0 = 2997.9\,h^{-1}$ Mpc is the Hubble radius, $T(k)$ is the matter transfer function, and $D(z)$ is the linear growth factor of matter perturbations normalized to unity at $z = 0$ (Dalal et al. 2008; Matarrese & Verde 2008; Slosar et al. 2008; Afshordi & Tolley 2008; McDonald 2008).[3] The numerical simulations by Dalal et al. (2008) have indeed shown that the halo bias is scale-dependent even for small values of k in non-Gaussian cosmologies (with $|f_{\rm NL}| = 100, 500$) and found qualitative agreement with equation (16). In Fig. 10, we show how the bias depends on scale in our simulations which also consider smaller values of $|f_{\rm NL}|$. Our results confirm the presence of a strongly scale-dependent bias. Larger values of $|f_{\rm NL}|$ correspond to a more marked scale dependence. Note, however, that for $k > 0.05\,h$ Mpc^{-1} the non-Gaussian deviation Δb changes sign. On these scales, the halo-matter and halo–halo spectra

[3] The factor $g(\infty)/g(0)$ is needed since Dalal et al. (2008) and Slosar et al. (2008) normalize the growth factor $D(z)$ to be $(1 + z)^{-1}$ during matter domination.

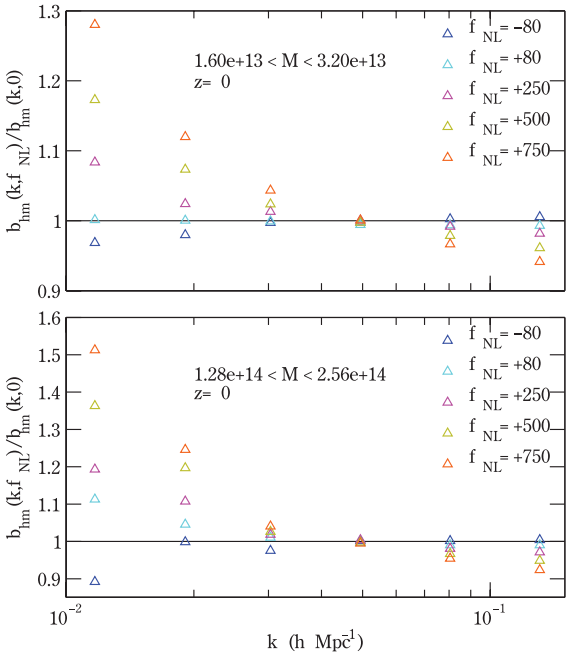

Figure 10. Scale-dependent halo bias arising from non-Gaussian initial conditions. Results are shown in terms of the ratio between the bias functions measured from a simulation with a given $f_{\rm NL}$ and with $f_{\rm NL} = 0$ at fixed halo mass (indicated by the label in units of $h^{-1}\,{\rm M}_\odot$). Note that in the Gaussian case the bias keeps nearly constant for $k < 0.05\,h$ Mpc^{-1}.

emerging from non-Gaussian perturbations has actually less power than in the Gaussian case. The opposite happens with the matter power spectrum (even to a larger degree) and the net effect is a negative Δb. This result implies that equation (16) can only hold asymptotically on very large scales. This is not surprising if interpreted within the peak-background-split formalism, where the large-scale bias is linked to the first derivative of the mass function with respect to σ^{-1}. In the non-Gaussian case, the bias is composed of two parts, a scale independent term and the correction given in equation (16). Since the halo mass function changes shape when $f_{\rm NL}$ is varied, also the constant bias should depend on $f_{\rm NL}$ for a fixed halo mass. Increasing $f_{\rm NL}$ corresponds to a larger abundance of massive haloes and to a slightly smaller constant bias with respect to the Gaussian case. Likely, this is what makes the Δb in the simulations negative for positive $f_{\rm NL}$. To proceed with a detailed analysis of our simulations, we find it convenient to rewrite equation (16) as

$$\Delta b = f_{\rm NL}\,(b_0 - 1)\,\frac{\Gamma}{\alpha(k, z)}\,, \tag{17}$$

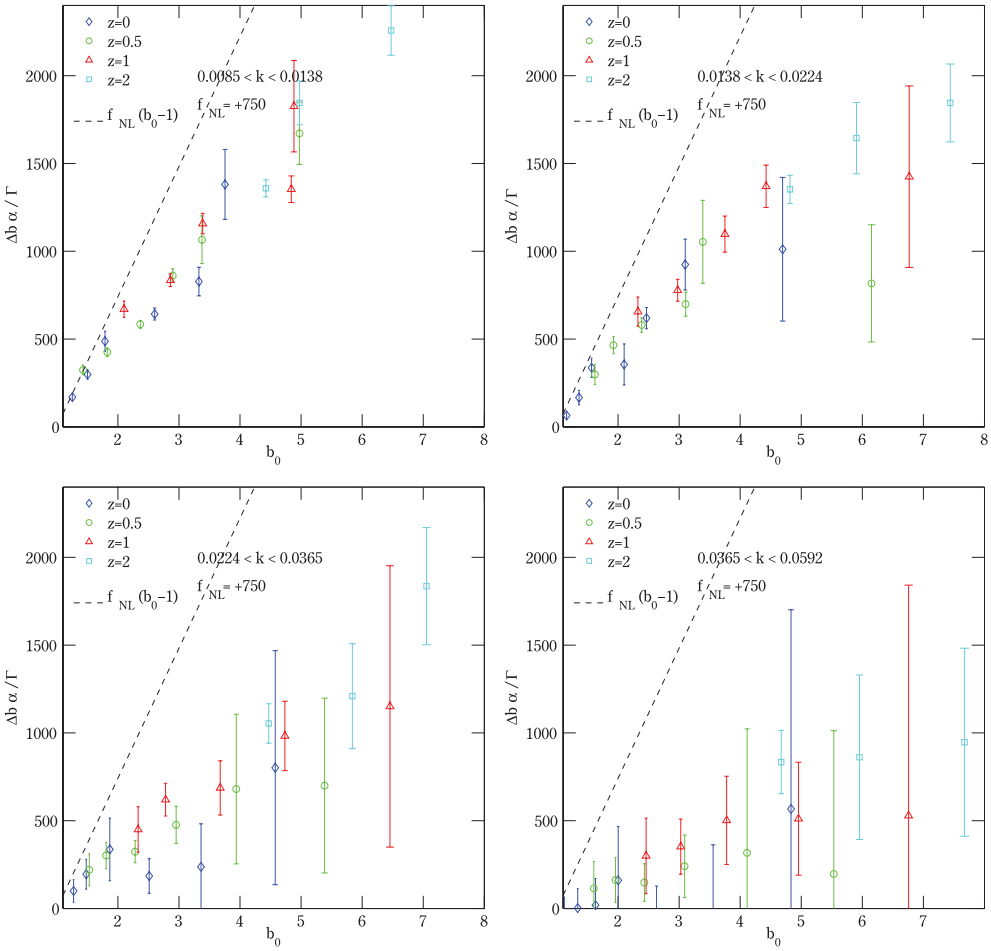

Figure 11. The non-Gaussian bias correction Δb as a function of the linear Gaussian bias b_0 for $f_{\rm NL} = 750$. Data from the simulations are indicated by symbols with errorbars and correspond to different redshifts as indicated in the label. The dashed line marks the prediction of the model in equation (16). The wavenumber in the labels is given in units of $h\,{\rm Mpc}^{-1}$. Horizontal errorbars are not drawn to improve readability.

where $\Gamma = 3\,\delta_{\rm c}\,\Omega_{\rm m}\,H_0^2/c^2$ and $\alpha(k,\,z) = k^2\,T(k)\,D(z)\,g(0)/g(\infty)$. In Fig. 11, we test the scaling of Δb with redshift, linear bias and wavenumber for $f_{\rm NL} = +750$ (where we have the best signal-to-noise ratio at high halo mass). Similar results are obtained with different values of $f_{\rm NL}$. The quantity shown is $\Delta b\,\alpha/\Gamma$ which should correspond to $f_{\rm NL}(b_0 - 1)$ if the analytical model provides a good description of the data. This quantity is indicated by a dashed line. The following two trends clearly emerge from the data. For small values of k, the model overestimates the data by 20–70 per cent increasing with b_0 and independently of z. On smaller scales, discrepancies become more and more severe. At $k \sim 0.05\,h\,{\rm Mpc}^{-1}$, the model is systematically a factor of 5 higher than the data. The k-dependence of Δb is therefore different from in equation (16).

The data also drop a hint that, for $k > 0.01\,h\,{\rm Mpc}^{-1}$, the scaling with $b_0 - 1$ might only persist up to a maximum value of b_0, $b_{0,\rm max}$. For $b_0 > b_{0,\rm max}$, it appears that the values of Δb are always smaller than expected from the extrapolation of the trend $b_0 - 1$ determined at smaller b_0. The value of $b_{0,\rm max}$ seems to depend both on redshift and wavenumber and roughly corresponds to constant halo mass for a given k. However, uncertainties in Δb at these high masses become very large, and it is difficult to judge how robust the existence of $b_{0,\rm max}$ really is. We note anyway that when we tried to fit data at different redshifts (for a given $f_{\rm NL}$ and $k > 0.015\,h\,{\rm Mpc}^{-1}$) by adding a variable normalization constant in front of equation (16), we systematically obtained significantly different fits (at a confidence level of $2.5\,\sigma$) at different redshifts. This trend disappears when only the lowest values of b_0 are considered at each redshift for the fit.

Data from simulations with all the considered values of $f_{\rm NL}$ are shown with different symbols and colours in Fig. 12. Each panel refers to a particular wavenumber bin (indicated by the label in units of $h\,{\rm Mpc}^{-1}$). The model in equation (16) is again indicated by a dashed line. Note that, in the most cases, it substantially deviates from the simulation data. In particular, Δb measured from the simulations shows a much stronger k-dependence than the analytical formula, as already seen in Fig. 11. In general, the overall amplitude of Δb drops by an extra factor of $\sim$3 with respect to $k^2\,T(k)$ when moving from $k \sim 0.01$ to $0.05\,h\,{\rm Mpc}^{-1}$ independently of b_0 and $f_{\rm NL}$. Also, Δb does not seem to scale linearly with $f_{\rm NL}$ while its linear dependence on $b_0 - 1$ appears to be solid, at least for $b_0 < b_{0,\rm max}$. We thus introduce a correcting factor $\beta(f_{\rm NL},\,k)$ defined by

$$\Delta b = \beta(f_{\rm NL},\,k)\,f_{\rm NL}\,(b_0 - 1)\,\frac{\Gamma}{\alpha(k,\,z)}, \qquad (18)$$

and we measure it by fitting the simulation data for $b(k,\,M,\,z,\,f_{\rm NL})$ and $b(k,\,M,\,z,\,0)$ at constant values of $f_{\rm NL}$ and k. We use an effective variance weighted least squares method to simultaneously account for errorbars on both bias parameters. The best-fitting values are

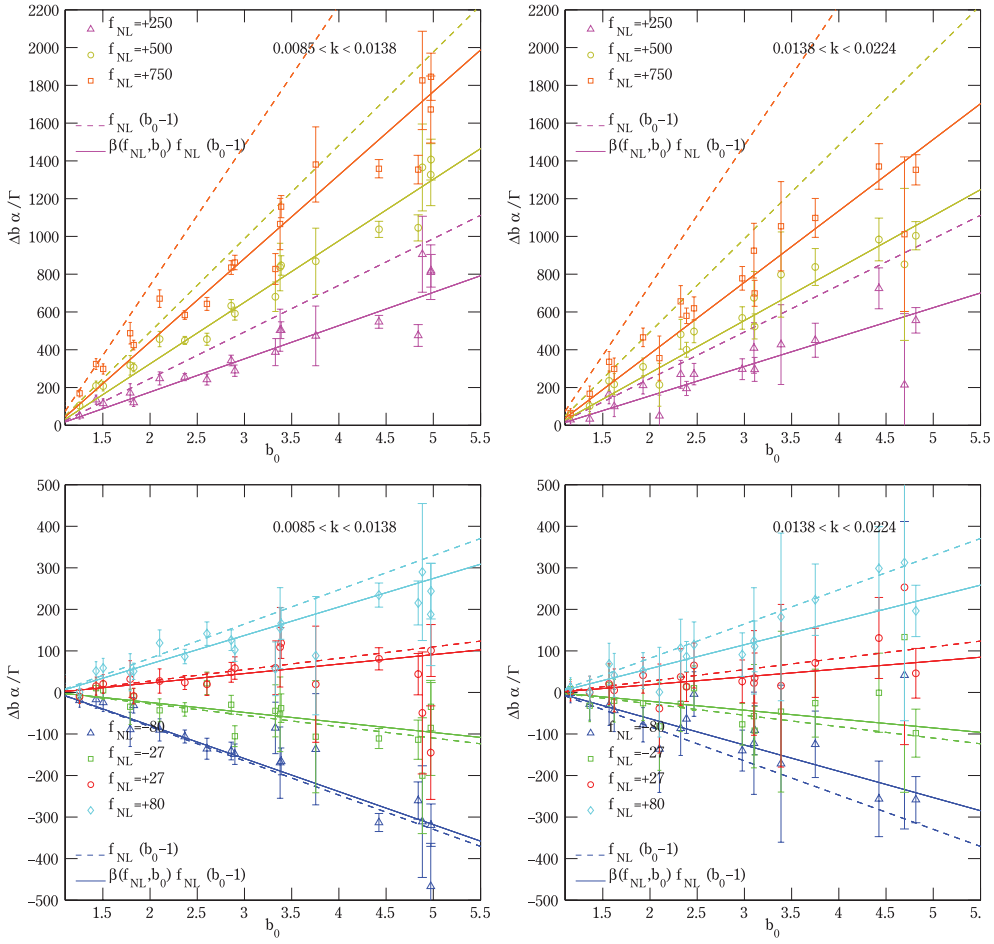

Figure 12. As in Fig. 11 but for all the simulations of our main series and without distinguishing data from different redshifts. The continuous line corresponds to our best-fitting values of β listed in Table 8.

Table 8. Best-fitting value and 1σ uncertainties for the multiplicative correction $\beta(k,\, f_{\rm NL})$. The first set of data corresponds to the k-interval where the Gaussian bias is constant.

$k(h\,{\rm Mpc}^{-1})$	$\beta(k,-80)$	$\beta(k,-27)$	$\beta(k,+27)$	$\beta(k,+80)$	$\beta(k,+250)$	$\beta(k,+500)$	$\beta(k,+750)$
0.0117	0.97 ± 0.04	0.88 ± 0.11	0.83 ± 0.13	0.83 ± 0.05	0.71 ± 0.02	0.66 ± 0.01	0.60 ± 0.01
0.0191	0.77 ± 0.07	0.78 ± 0.21	0.69 ± 0.25	0.70 ± 0.10	0.63 ± 0.03	0.56 ± 0.01	0.51 ± 0.01
0.0303	0.65 ± 0.14	0.58 ± 0.27	0.59 ± 0.27	0.54 ± 0.16	0.50 ± 0.06	0.42 ± 0.03	0.37 ± 0.02
0.0494	0.35 ± 0.32	0.45 ± 0.19	0.40 ± 0.26	0.31 ± 0.33	0.29 ± 0.09	0.25 ± 0.05	0.20 ± 0.02
0.0804	0.01 ± 0.23	0.20 ± 0.21	-0.10 ± 0.43	-0.06 ± 0.22	-0.08 ± 0.18	-0.10 ± 0.09	-0.11 ± 0.04

reported in Table 8 and can be used to compute the function β by interpolation. The final expression for Δb, corrected with the β factor, is shown in Fig. 12 with solid lines.

Data in Table 8 have an amazing regularity. Apart from a normalization constant, each column (row) shows the same linear trend with k ($f_{\rm NL}$). This suggests that, within the explored parameter range ($0.01 < k < 0.05\,h\,{\rm Mpc}^{-1}$ and $-80 \le f_{\rm NL} \le 750$),

$$\beta(k,\, f_{\rm NL}) = \beta_0\,(1-\beta_1\,f_{\rm NL})\,(1-\beta_2\,k)\ . \qquad (19)$$

We thus use this equation to fit the original data for the halo bias from Gaussian and non-Gaussian initial conditions and find

$$\begin{aligned}\beta_0 &= 1.029 \pm 0.027\ ,\\ \beta_1 &= (4.25 \pm 0.33) \times 10^{-4}\ ,\\ \beta_2 &= 14.8 \pm 0.5\ h^{-1}\,{\rm Mpc}\ ,\end{aligned} \qquad (20)$$

at the 68.3 per cent confidence level. Note that we computed the power spectra in finite-sized bins of the wavenumber, so that there is some degree of ambiguity in associating the results with a given value of k. Unfortunately, the choice plays a role in determining β as α is a steep function of k on the scales of interest. In Table 8 and equation (20), we have used the arithmetic mean of the wavenumbers contributing to a given bin. If one instead uses the logarithmic centre of the bin, β_0 is slightly reduced with a best-fitting value of 0.897 ± 0.024. The parameters β_1 and β_2 are unaltered. Therefore, a systematic contribution $\simeq 0.1$ should be added to the error budget of β_0.

Equations (16) and (18) assume that the Gaussian bias b_0 is constant with k but this is only approximately true in the simulations. The fit in equation (20), Table 8 and Figs 11 and 12 have been obtained by identifying b_0 with the actual bias measured in the

Gaussian simulation at each wavenumber. If, instead, the estimate for b_0 introduced in Section 5.1 is used, one gets $\beta_0 = 0.970 \pm 0.027$, $\beta_1 = (4.13 \pm 0.33) \times 10^{-4}$ and $\beta_2 = 13.8 \pm 0.7\,h^{-1}\,\mathrm{Mpc}$, slightly improving the goodness of the fit.

The quadratic dependence of Δb on $f_{\rm NL}$ is rather surprising as it cannot be straightforwardly derived from the simple models listed above. It might possibly arise from higher order terms which have been neglected in the expansion that leads to equation (16). Anyway, it is clearly present in the simulations as it can be seen by looking at the variation of β along a given row in Table 8. Within the range of $f_{\rm NL}$ of physical interest, the effect is rather small: the coefficient β_1 only corresponds to a few percent correction. Note that a quadratic term breaks the symmetry in the amplitude of Δb between non-linearity parameters with opposite sign and identical absolute value. It is hard to directly test this against our simulations as we just have two runs with $f_{\rm NL} < 0$ and both of them correspond to rather small $|f_{\rm NL}|$ where the uncertainties in β are large. An alternative explanation for a non-vanishing β_1 could be that it artificially derives from imposing a linear relation in $b_0 - 1$ to data that do not scale linearly for $b_0 > b_{0,\rm max}$. Indeed, just using data points with small values of b_0 we derive bigger values of β for large $f_{\rm NL}$ (more or less in line with $\beta_1 = 0$). Therefore, what is robust is that at least one of the scalings with b_0 or with $f_{\rm NL}$ is incorrect in equation (16). We found that a scaling proportional to $\gamma_0(1 + \gamma_1 \log b_0)$ (with γ_0 and γ_1 two adjustable parameters) does slightly better (in terms of reduced χ^2) than $\beta_0(b_0 - 1)$, at least for $k > 0.014\,h\,\mathrm{Mpc}^{-1}$. However, since the scaling with $b_0 - 1$ has a sound theoretical basis (Mo & White 1996; Catelan et al. 1998), we preferred to quote our results as in equation (19). From the statistical point of view, the parameters (20) provide an acceptable description of the simulation data to high confidence for all values of b_0. However, they are particularly accurate for $b_0 > 2 - 2.5$, while $\beta_1 \sim 0$ (with the same β_0 and β_2) has to preferred for smaller values of b_0.

The linear correction in k should be thought of as the first-order term of a series expansion in the wavenumber. We attempted to determine the corresponding quadratic term by considering larger values of k in the fit (one bin more, up to $k = 0.0962\,h\,\mathrm{Mpc}^{-1}$). However, values of Δb become small compared with the numerical errors, and we found that the quadratic parameter is badly constrained by the data ($\beta_3 = 34 \pm 34\,h^{-2}\,\mathrm{Mpc}^2$) while the other parameters remain nearly unchanged (and get larger uncertainties). Also note that the Gaussian bias starts to depart from b_0 at $k > 0.05\,h\,\mathrm{Mpc}^{-1}$ and it is not clear whether equation (16) should still be expected to hold in this regime.

Dalal et al. (2008) derived an expression for Δb which coincides with equation (16) but does not include the linear transfer function. Theoretically, this is hard to understand, as non-Gaussianity is generated well before matter-radiation equality and one should account for the linear evolution of density perturbations. Anyway, due to the different k-dependence, their expression for Δb provides a better fit to the simulation data than equation (16) when both models are allowed to vary in amplitude with a tunable free parameter.[4] None of them, however, provides such an accurate fit to the data as our equations (19) and (20), which improve the χ^2 by at least a factor of 1.7.

[4] The best-fitting value for this coefficient reads 0.92 for the model of Dalal et al. (2008) and 0.58 for the model of Slosar et al. (2008)

6 DISCUSSION

Slosar et al. (2008) have used equation (16) to constrain $f_{\rm NL}$ by considering measures of the clustering amplitude of LRGs and quasars from the SDSS. Combining all data sets, they found $-29 < f_{\rm NL} < +70$ at 95 per cent confidence. How would this result change based on our simulations? Disentangling the different contributions, the strongest constraints to $f_{\rm NL}$ in Slosar et al. (2008) come from the angular power spectrum of quasars with photometric redshifts in the range $1.45 < z < 2.00$ and a mean bias of $\sim$2.7. Weaker limits are also contributed from the power spectrum of spectroscopic LRGs and the angular spectrum of photometric LRGs (with a bias of $\sim$2 at $z \sim 0.5$). Fig. (12) and Table 8 suggest that at the scales of interest ($0.01 < k < 0.05\,h\,\mathrm{Mpc}^{-1}$) the model given in equation (16) tends to overestimate the scale-dependent bias seen in the simulations. Therefore, to match an observed Δb, a larger value of $|f_{\rm NL}|$ is required than predicted by the analytic model. When applied to the data by Slosar et al. (2008), our correction should thus give somewhat looser limits on $f_{\rm NL}$. Because of the strong k-dependence of the function β it is impossible to give more precise estimates without fitting the power-spectrum data. Note, however, that a steeper k-dependence potentially makes determinations of $f_{\rm NL}$ even more competitive with respect to studies of CMB anisotropies.

7 SUMMARY

We use a series of high-resolution N-body simulations to study the mass function and the clustering properties of dark-matter haloes arising from Gaussian and non-Gaussian initial conditions. In particular, we follow the formation of structure in a universe characterized by the best-fitting parameters from the third- and fifth-year *WMAP* data releases. We consider non-Gaussianity of the local type and we use eight different values of $f_{\rm NL}$ (-80, -27, 0, $+27$, $+80$, $+250$, $+500$, $+750$) enclosing the parameter space currently allowed by studies of the CMB. Our main results can be summarized as follows.

(i) The mass function of dark-matter haloes varies with $f_{\rm NL}$. Larger values of the non-linearity parameter correspond to higher abundances of the most massive haloes. Analytical models based on the Press–Schechter method (Matarrese et al. 2000; LoVerde et al 2008) are compatible with our simulated results for the ratio of the Gaussian and non-Gaussian mass functions only if the critical threshold for halo collapse is lowered to $\delta_{\rm c} \sim 1.5$. An accurate fit of the Gaussian $\mathrm{d}n/\mathrm{d}M$ is necessary to derive the non-Gaussian mass function from the aforementioned ratio.

(ii) We find that, in perfect analogy with the Gaussian case (Jenkins et al. 2001), the halo mass function assumes an approximately universal form. This means that, when expressed in terms of suitable variables, its dependence on redshift and cosmology is erased to good precision (nearly 10 per cent). We parametrize the $f_{\rm NL}$-dependence of the universal mass function and provide an accurate fit for its high-mass end. For $-80 \leq f_{\rm NL} \leq 250$ and for masses $M > 10^{13}\,h^{-1}\,\mathrm{M}_\odot$, the best-fitting parameters for the non-Gaussian halo mass function in equation (4) are given in equation (7) and Table 4. This fit reproduces the mass function of FOF haloes with an accuracy of 5 per cent on top of a systematic contribution (up to 10 per cent) due to the non-perfect universality. For applications requiring higher precision, an additional formula is provided: for $-80 \leq f_{\rm NL} \leq 80$ and $0 \leq z \leq 0.5$, the fit in equations (10), (4) and (11) has to be preferred to the universal fit. On the other hand, for higher values of $|f_{\rm NL}|$ and for higher redshifts, the universal fit gives a

better and more economic (in terms of parameters) description of the data.

In the Gaussian case, we extend the fit to a larger interval of halo masses ($M > 2.4 \times 10^{10}\,h^{-1}\,\mathrm{M}_{\odot}$) by combining simulations with different box sizes – see equations (4) and (5). Our fitting function provides a precious tool to forecast constraints on $f_{\rm NL}$ from future surveys and to analyse current data sets.

(iii) The matter power spectrum in non-Gaussian cosmologies departs from the Gaussian one already on very large scales. For values of $f_{\rm NL}$ within the current CMB constraints these scale-dependent deviations can be as high as two per cent at $k = 0.3\,h\,\mathrm{Mpc}^{-1}$ and increase with wavenumber. The discrepancy is systematic: models with positive $f_{\rm NL}$ have more large-scale power than the Gaussian case and models with negative $f_{\rm NL}$ have less. This warns against the widespread habit of using the Gaussian matter power spectrum to determine non-Gaussian bias parameters when high-precision is required. It also suggests that primordial non-Gaussianity modifies the shape and amplitude of the baryonic-oscillation feature in the two-point statistics and the convergence power spectrum in weak-lensing studies.

(iv) We present an accurate fitting formula for the linear bias of dark matter haloes arising from Gaussian initial conditions extending previous work to larger mass intervals. This, together with the mass function fit mentioned above, can be used to constrain parameters of halo-occupation models from clustering data.

(v) Finally, using the halo-matter cross-spectrum, we confirm the strong k-dependence of the halo bias on large scales ($k < 0.05\,h\,\mathrm{Mpc}^{-1}$) which was already detected by Dalal et al. (2008). However, we show that commonly used parametrizations based on the peak-background split overestimate the effect for $k > 0.01\,h\,\mathrm{Mpc}^{-1}$. The discrepancy increases with the wavenumber and at $k > 0.05\,h\,\mathrm{Mpc}^{-1}$ Δb in the simulations changes sign with respect to the models. On top of this, the analytic model for the scale-dependent part of the bias requires corrections which depend on the non-linearity parameter, the wavenumber and, possibly, also on redshift and clustering strength. equations (18) and (19) with the best-fitting parameters listed in (20) provide a fitting formula which accurately reproduces the outcome of the simulations for $0.01 < k < 0.05\,h\,\mathrm{Mpc}^{-1}$ and $-80 \leq f_{\rm NL} \leq 750$. This fit should be employed to constrain $f_{\rm NL}$ from future clustering data at low and high redshift.

ACKNOWLEDGMENTS

All simulations were performed at the Swiss National Supercomputing Center (CSCS) in Manno, Switzerland. AP and OH acknowledge support from the Swiss National Science Foundation. We thank Volker Springel for kindly making the lean version of the GADGET-2 code available to us. We acknowledge discussions with Robert E. Smith and Tommaso Giannantonio. While our paper was being submitted, a related work by Desjacques, Seljak & Iliev (2008) appeared as a pre-print. Their results based on a different halo finder are in qualitative agreement with ours with the exception of the non-Gaussian bias correction for small halo masses ($b_0 < 1.5$) which they find to exceed the model by Slosar et al. (2008).

REFERENCES

Afshordi N., Tolley A. J., 2008, Phys. Rev. D, 78, 123507
Amara A., Refregier A., 2004, MNRAS, 351, 375
Bardeen J. M., Bond J. R., Kaiser N., Szalay A. S., 1986, ApJ, 304, 15
Bartolo N., Komatsu E., Matarrese S., Riotto A., 2004, Phys. Rep., 402, 103
Bartolo N., Matarrese S., Riotto A., 2005, J. Cosmol. Astropart. Phys., 10, 010
Bertschinger E., 2001, ApJS, 137, 1
Bond J. R., Cole S., Efstathiou G., Kaiser N., 1991, ApJ, 379, 440
Buchbinder E. I., Khoury J., Ovrut B. A., 2008, Phys. Rev. Lett., 100, 171302
Catelan P., Lucchin F., Matarrese S., Porciani C., 1998, MNRAS, 297, 692
Carbone C., Verde L., Matarrese S., 2008, ApJ, 684, 1
Cohn J. D., White M., 2008, MNRAS, 385, 2025
Cooray A., 2006, Phys. Rev. Lett., 97, 261301
Creminelli P., Senatore L., 2007, J. Cosmol. Astropart. Phys., 11, 010
Creminelli P., Senatore L., Zaldarriaga M., 2007, J. Cosmol. Astropart. Phys., 03, 19
Crocce M., Pueblas S., Scoccimarro R., 2006, MNRAS, 373, 369
Curto A., Martinez-Gonzalez E., Mukherjee P., Barreiro R. B., Hansen F. K., Liguori M., Matarrese S., 2008, MNRAS, in press
Dalal N., Dore' O., Huterer D., Shirokov A., 2008, Phys. Rev. D, 77, 123514
Desjacques V., Seljak U., Iliev I. T., 2009, MNRAS, 396, 85
Evrard A. E. et al., 2002, ApJ, 573, 7
Falk T., Rangarajan R., Srednicki M., 1993, ApJ, 403, 1
Gangui A., Lucchin F., Matarrese S., Mollerach S., 1994, ApJ, 430, 447
Grinstein B., Wise M. B., 1986, ApJ, 310, 19
Grossi M., Dolag K., Branchini E., Matarrese S., Moscardini L., 2007, MNRAS, 382, 1261
Grossi M., Branchini E., Dolag K., Matarrese S., Moscardini L., 2008, MNRAS, 390, 438
Grossi M., Verde L., Carbone C., Dolag K., Branchini E., Iannuzzi F., Matarrese S., Moscardini L., 2009, MNRAS, 398, 321
Heitmann K., Lukić Z., Habib S., Ricker P. M., 2006, ApJ, 642, 85
Hikage C., Matsubara T., Coles P., Liguori M., Hansen F. K., Matarrese S., 2008, MNRAS, 389, 1439
Huterer D., Takada M., 2005, Astropart. Phys., 23, 369
Jenkins A., Frenk C. S., White S. D., Colberg J. M., Cole S., Evard A. E., Couchman H. M. P., Yoshida N., 2001, MNRAS, 321, 372
Jeong E., Smoot G. F., 2007, preprint (arXiv:0710.2371)
Jing Y. P., 1998, ApJ, 503, L9
Kang X., Norberg P., Silk J., 2007, MNRAS, 376, 343
Knebe A., Wagner C., Knollmann S., Diekershoff T., Krause F., 2009, ApJ, 698, 266
Komatsu E., Spergel D. N., 2001, Phys. Rev. D, 63, 063002
Komatsu E. et al., 2009, ApJ, 180, 330
Koyama K., Soda J., Taruya A., 1999, MNRAS, 310, 1111
Lehners J.-L., Steinhardt P. J., 2008, Phys. Rev. D, 77, 063533
Linde A., Mukhanov V., 1997, Phys. Rev. D, 56, 535
LoVerde M., Miller A., Shandera S., Verde L., 2008, J. Cosmol. Astropart. Phys., 04, 014
Lucchin F., Matarrese S., Vittorio N., 1988, ApJl, 330, L21
Lukić Z., Heitmann K., Habib S., Bashinsky S., Ricker P. M., 2007, ApJ, 671, 1160
McDonald P., 2008, Phys. Rev. D, 78, 123519
Magliocchetti M., Porciani C., 2003, MNRAS, 346, 186
Maldacena J., 2003, J. High Energy Phys., 05, 013
Matarrese S., Verde L., 2008, ApJ, 677, L77
Matarrese S., Lucchin F., Bonometto S. A., 1986, ApJ, 310, L21
Matarrese S., Verde L., Jimenez R., 2000, ApJ, 541, 10
Mo H. J., White S. D. M., 1996, MNRAS, 282, 347
Moscardini L., Matarrese S., Lucchin F., Messina A., 1991, MNRAS, 248, 424
Peebles P. J. E., 1980, The Large Scale Structure of the Universe, Research supported by the National Science Foundation. Princeton Univ. Press, Princeton, N.J.
Pillepich A., Porciani C., Matarrese S., 2007, ApJ, 662, 1
Porciani C., Catelan P., Lacey C., 1999, ApJ, 513, L99
Press W. H., Schechter P., 1974, ApJ, 187, 425
Pyne T., Carroll S. M., 1996, Phys. Rev. D, 53, 2920
Reed D., Gardner J., Quinn T., Stadel J., Fardal M., Lake G., Governato F., 2003, MNRAS, 346, 365
Robinson J., Baker J. E., 2000, MNRAS, 311, 781
Robinson J., Gawiser E., Silk J., 2000, ApJ, 532, 1

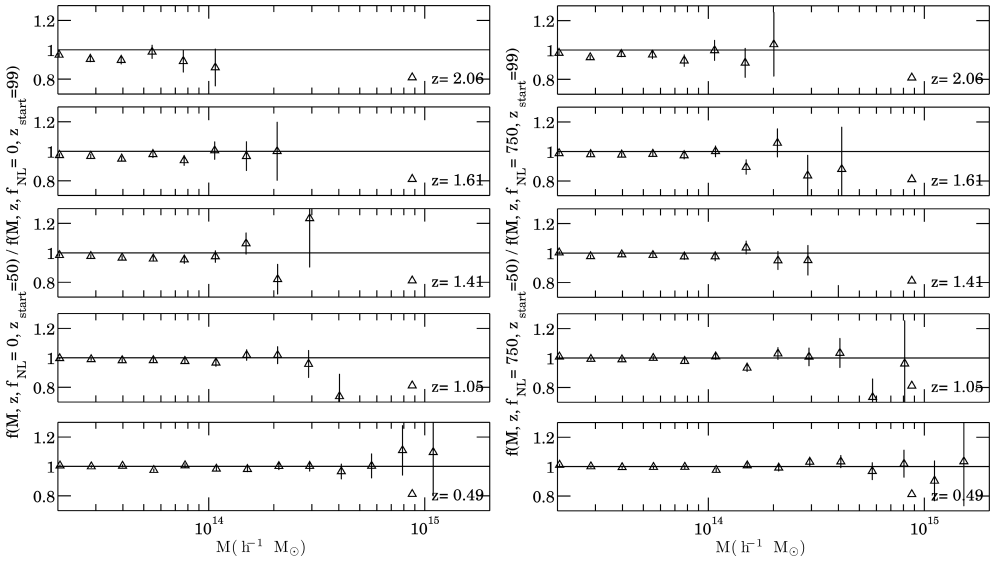

Figure A1. Effect of the initial redshift $z_{\rm start}$ on the halo mass-function, for $f_{\rm NL} = 0$ (left-hand panel) and $f_{\rm NL} = +750$ (right-hand panel).

Salopek D. S., Bond J. R., 1990, Phys. Rev. D, 42, 3936
Scoccimarro R., Sefusatti E., Zaldarriaga M., 2004, Phys. Rev. D, 69, 103513
Sefusatti E., Komatsu E., 2007, Phys. Rev. D, 76, 083004
Seljak U., Warren M. S., 2004, MNRAS, 355, 129
Sheth R. K., Tormen G., 1999, MNRAS, 308, 119
Sheth R. K., Mo H. J., Tormen G., 2001, MNRAS, 323, 1
Slosar A., Hirata C., Seljak U., Ho S., Padmanabhan N., 2008, J. Cosmol. Astropart. Phys., 08, 031
Smith R. E., 2009, MNRAS, 400, 85
Smith R. E., Scoccimarro R., Sheth R. K., 2007, Phys. Rev. D, 75, 3512
Spergel D. N. et al., 2007, ApJS, 170, 377
Springel V., 2005, MNRAS, 364, 1105
Stanek R., Rudd D., Evrard A. E., 2009, MNRAS, 394, 11
Taruya A., Koyama K., Matsubara T., 2008, Phys. Rev. D, 78
Tinker J. L., Weinberg D. H., Zheng Z., Zehavi I., 2005, ApJ, 631, 41
Tinker J. L., Kravtsov A. V., Klypin A., Abazajian K., Warren M. S., Yepes G., Gottlober S., Holz D. E., 2008, ApJ, 688, 709
Verde L., Wang L., Heavens A. F., Kamionkowski M., 2000, MNRAS, 313, 141
Warren M. S., Abazajian K., Holz D. E., Teodoro L., 2006, ApJ, 646, 881
White M., 2002, ApJS, 143, 241
Willick J. A., 2000, ApJ, 530, 80
Yadav A. P. S., Wandelt B. D., 2008, Phys. Rev. Lett., 100, 181301
Zel'dovich Y. B., 1970, A&A, 5, 84

APPENDIX A: INITIAL CONDITIONS AND ZEL'DOVICH TRANSIENTS

The initial positions and velocities of the particles in our N-body simulations have been generated using the Zel'dovich approximation. This method introduces long-lasting artificial transients in the growth of perturbations which might alter the halo mass function at the high-mass end even at very late epochs (Crocce, Pueblas & Scoccimarro 2006). It is therefore important to start the simulation at a sufficiently high redshift to ensure that all transients have decayed within the cosmic time at which the simulation output is used for science applications. Alternatively, less stringent requirements on the initial redshift are necessary if one uses second-order Lagrangian perturbation theory to displace particles at the initial time (Crocce et al. 2006).

The simpler Zel'dovich approximation (which only requires the calculation of the gravitational potential) is much more widespread. In this case, a few authors have investigated how to compute the optimal starting redshift (see e.g. Lukić et al. 2007) as well as quantified the effects of the initial redshift on the halo mass function (Tinker et al. 2008) and on the internal properties of dark matter haloes (Knebe et al. 2009). These studies show that simulations of the concordance cosmology (and Gaussian initial conditions) with initial redshifts of $35 < z_{\rm start} < 60$ (depending on the simulations specifications) have converged to the correct solution by $z = 0$ (at least for halo masses $M < 10^{14}\,h^{-1}\,{\rm M}_{\odot}$). Even though our $z_{\rm start}$ is in the right ball park, it is important to test that our results are robust against changing initial redshift. We thus decided to perform the following simple test: we re-simulated Run1.0 and Run1.750 of our main Series using $z_{\rm start} = 99$ instead of $z_{\rm start} = 50$ and compared the halo mass functions of the two simulations as a function of redshift (see Fig. A1). In good agreement with Tinker et al. (2008), for $f_{\rm NL} = 0$ we find that discrepancies are smaller than 10 per cent at $z \sim 2$ and that the (possible) effects of Zel'dovich transients are completely erased by $z \sim 1$. Our results show that this holds true also for relatively large values of $f_{\rm NL}$ (see the right-hand panel in Fig. A1 where $f_{\rm NL} = +750$): even though non-linearities in the initial conditions are slightly enhanced with respect to the Gaussian case, at any given redshift the corresponding density field is also more evolved and the effect of the Zel'dovich transients on the halo mass function are again erased by $z \sim 2$. For this reason, this paper only uses data from snapshots at $z \leq 1.6$ which are accurate to better than 5 per cent.

This paper has been typeset from a TEX/LATEX file prepared by the author.